

X-rays profiles in symmetric and asymmetric supernova remnants

L. Zaninetti¹

¹ *Dipartimento di Fisica Generale, Via Pietro Giuria 1,
10125 Torino, Italy
E-mail: zaninetti@ph.unito.it*

Received 2005 April 10; revised 2005 June 14

Abstract. The non-thermal X-rays from the SN 1006 NE rim present characteristic scale lengths that are interpreted in the context of diffusion of a relativistic electron. The adopted theoretical framework is the mathematical diffusion in 3D, 1D and 1D with drift as well as the Monte Carlo random walk in 1D with drift. The asymmetric random walk with diffusion from a plane can explain the scale widths of 0.04 pc upstream and 0.2 pc downstream in the non thermal intensity of X-ray emission in SN 1006. A mathematical image of the non thermal X-flux from an supernova remnant as well as profiles function of the distance from the center can be simulated. This model provides a reasonable description of both the limbs and the central region of SN 1006. A new method to deduce the magnetic field in supernova remnant is suggested.

Key words: (ISM:) supernova remnants ; X-rays: general ;

1. Introduction

In order to explain the non-thermal emission from astrophysical objects and the energy distribution of cosmic rays, the theory of particle acceleration was developed using various types of acceleration mechanisms, of which some are briefly reviewed as follows :

- acceleration from Interstellar Medium (in the following ISM) irregularities, Fermi (1949)
- magnetic pumping , Parker (1958)
- strong shocks , Krymskii (1977) , Axford et al. (1978) , Blandford & Ostriker (1978) , Bell (1978a) , Bell (1978b) and the detailed review of Drury (1983)
- scattering by hydro-magnetic waves , Skilling (1975).

At the same time, the transport equation for the electron energy was set up , see for example Parker (1965) , Kirk (1994) , Jokipii (1987) and Berezhinskii et al. (1990) .

Further on, recent developments in the quasi-linear theory of particle acceleration by super-Alfvénic shock waves (see for example Vainio & Schlickeiser (1998)

, Klepach et al. (2000) and Schlickeiser (2002) for a general review) produced detailed results on the spatial diffusion coefficient but did not cover the possibility of simulating the X-contours of the astrophysical object. We briefly review the effects on electron transport that are due to the dynamic nature of a scatterer, see for example Skilling (1975), equation (9):

- convection of electrons with the bulk flow of the plasma
- adiabatic cooling/heating of electrons in regions of diverging/converging flow
- stochastic acceleration of electrons

While the last effect may be considered small under some relatively reasonable restrictions, the first and second effects are important ingredients in the standard transport equation of electrons. The effect of convection would be to cause asymmetry in the modelled X-contours by pressing them closer together on the upstream side and further away from each other on the downstream side of the source. But these two effects require the residence time of relativistic electrons in the emitting layer to be greater than the adiabatic/convection time: if this inequality is not verified these two effects are negligible.

The Monte Carlo modelling of particle acceleration and transport is not a new concept and has been extensively used in supernova remnant (in the following SNR), in particular:

- Calculations of test particle spectra and acceleration times are analysed in Ellison et al. (1990) by adopting a first-order Fermi particle acceleration for parallel shocks with arbitrary flow velocities and compression ratios r up to seven, shock velocities u_1 up to $0.98c$, and injection energies ranging from thermal to highly super-thermal.
- Calculations concerning the ion and electron spectra produced by Fermi acceleration in a steady state plane parallel modified shock for Mach numbers of 170 and 43 are reported in Ellison & Reynolds (1991).
- An extended simple model of nonlinear diffusive shock acceleration was developed by Ellison et al. (2000) and includes the injection and acceleration of electrons, the production of photons from bremsstrahlung, synchrotron, inverse-Compton, and pion-decay processes.
- X-ray emission in the supernova remnant G347.3-0.5 is explained by an electron population generated by diffusive shock acceleration at the remnant forward shock, see Ellison et al. (2001).

In astrophysics we see synchrotron emission from places other than the sites of active acceleration. It is therefore a question of electron transport and in this paper the following questions are posed:

- The trajectory of the relativistic electron that produces synchrotron radiation is helicoidal: on which scales can the trajectory be approximated by a rectilinear motion?
- How can a theory of a particle that diffuses through the random walk be developed when the mathematical diffusion is adopted?

- The relativistic electrons alone produce e.m. radiation at a given observing frequency but the spatial gradients that characterise the X–sources require another treatment. Could a theory that simulates the contours of non-thermal X–emission be set up?
- Can a theory of diffusion from a plane in the presence of convection be set up?
- The X–contours of many SNR (for example Cas A, Tycho and SN 1006) present a ring enhancement of the intensity toward the external zones: does the observed ring have a theoretical explanation and can it be simulated?

The trajectories adopted in diffusing away from the center of the box were described in Sect. 2.3.

The mathematical diffusion with and without the convection was set up in Sect. 3.

The physical bases of the random walk for relativistic electrons was introduced in Sect. 4.

The Monte Carlo experiment that simulates the diffusion of relativistic electrons from a plane in the presence of a stationary state situation was carried out in Sect. 5.

The formula that allows the theoretical counterpart of the intensity of radiation to be built was developed in Sect. 6; this mathematical intensity explains the observed X-flux enhancement in the ring of many SNR.

The two asymmetries in the observed flux are explained with an energy cascade function of the field of radial velocities among the various regions of the SNR, see Sect. 6.6.

2. Synchrotron X-ray emission in astrophysical objects

When X-ray observations from satellites like Einstein, Chandra and ASCA are directed toward typical astrophysical objects like SNR, super-bubbles and extragalactic radio–sources, they detect non thermal emission with intensity $I(\nu) \propto \nu^{-\alpha}$ (here ν is the frequency and α the power law index), see for example Pacholczyk (1970). The SNR, in particular, presents sharp boundaries in the observed flux that can be explained by invoking drift effects. On adopting standard values of the magnetic field, the gyro-radius of emitting regions turns out to be ≈ 200 times smaller than the typical dimensions where the emission is thought to originate. This fact allows us to build a theory of electron transport with a step length 2 decades smaller than the source dimension.

These observational effects offer a starting point with which

- to analyse the random walk performed with steps of a physical dimension $\frac{side(pc)}{(NDIM-1)}$, where *side* represents the dimension of the considered box and NDIM the number of mean free paths contained in the box,
- the computation of the synchrotron losses at the light of the random walk,
- the setting of the radiative transfer equation,
- to group all the data on SNR in a unique section.

2.1. Synchrotron emission and losses

Once the relativistic electrons are accelerated (see Appendix A for a brief review on the acceleration mechanism), the synchrotron losses due to the magnetic field are:

$$\frac{dE}{dt} = -b_{rad} E^2 \quad \text{erg sec}^{-1} \quad , \quad (1)$$

in cgs E is expressed in ergs , $b_{rad} = 1.579 \times 10^{-3} H^2$ and H is expressed in Gauss. Another type of loss is the adiabatic one, but in Appendix B we have shown that they can be neglected because the residence times of the relativistic electrons are small.

We will see in Sect. 4.2.2 that the synchrotron losses are negligible in the X-region and consequently the working hypothesis of the random walk without losses is justified.

2.2. Radiative transfer equation

The transfer equation in the presence of emission only , see for example Rybicki & Lightman (1985) or Hjellming (1988) , is

$$\frac{dI_\nu}{ds} = -k_\nu \zeta I_\nu + j_\nu \zeta \quad , \quad (2)$$

where I_ν is the specific intensity , s is the line of sight , j_ν the emission coefficient, k_ν a mass absorption coefficient, ζ the mass density at position s and the index ν denotes the interested frequency of emission. The solution of equation (2) is

$$I_\nu(\tau_\nu) = \frac{j_\nu}{k_\nu} (1 - e^{-\tau_\nu(s)}) \quad , \quad (3)$$

where τ_ν is the optical depth at frequency ν

$$d\tau_\nu = k_\nu \zeta ds \quad . \quad (4)$$

The synchrotron emission values of $j_\nu \zeta$ and $k_\nu \zeta$ can be found in Hjellming (1988) . We now continue analysing the case of optically thin layer in which τ_ν is very small (or k_ν very small) and the density ζ is substituted with our concentration $C(s)$ of relativistic electrons

$$j_\nu \zeta = K_e C(s) \quad , \quad (5)$$

where K_e is a constant function of the energy power law index, the magnetic field and the frequency of e.m. emission. The intensity is now

$$I_\nu(s) = K_e \int_{s_0}^s C(s') ds' \quad \text{optically thin layer} \quad . \quad (6)$$

The increase in brightness is proportional to the concentration integrated along the line of sight. In Monte Carlo experiments the concentration is memorised on the grid \mathcal{M} and the intensity is

$$I(i, j) = \sum_k \Delta s \times \mathcal{M}(i, j, k) \quad \text{optically thin layer} \quad , \quad (7)$$

where Δs is the spatial interval between the various values and the sum is performed over the interval of existence of the index k . The theoretical flux density is then obtained by integrating the intensity at a given frequency over the solid angle of the source. In order to deal with the transition to the optically thick case in the Monte Carlo simulation, see Sect.6.2, the intensity is given by

$$I(i, j) = \frac{1}{K_a} (1 - \exp(-K_a \sum_k \Delta s \times \mathcal{M}(i, j, k))) \quad \text{thin} \mapsto \text{thick} \quad , \quad (8)$$

where K_a is a constant that represents the absorption. Performing a Taylor expansion of the last formula (8), the equation (7) is obtained.

2.3. The trajectories

Here the approximation of trajectories moving on a straight line is used and the randomisation on the two or six main directions is due to the presence of scattering clouds (without re-acceleration), see Appendix A. The length of the step δ is now compared with the length where the standard theories assume that the transport is working. If the magnetic field is strongly turbulent, the mean free path of an electron can be identified with its gyro-radius. The gyro-radius of the electron can be parametrised by using the synchrotron emission frequency expressed in MHz units, ν_M , and the magnetic field expressed in 10^{-4} Gauss units, H_{-4} :

$$\rho = 2.6 \cdot 10^{-10} \frac{(\nu_M)^{1/2}}{(H_{-4})^{3/2}} pc \quad . \quad (9)$$

This should be considered an approximate relationship since even a single electron produces an emission spectrum of finite width. On the insertion of the magnetic field of SN 1006, $H_{-4} = 0.15$ (see discussion on the data of SN 1006 in Sect. 2.4) the value of the gyro-radius now depends exclusively on the chosen emission frequency. A typical frequency belonging to the radio-window is 1 GHz which corresponds to $\rho = 0.141 \cdot 10^{-6}$ pc. The thickness of the emitting shell is 0.52 pc which means that NDIM should be $3.6 \cdot 10^6$ once we assume that the length of the step is equal to the gyro-radius.

Another zone of the e.m. spectrum analysed here is X-ray emission, see Sect. 6. In this case the frequency observed is $4 \cdot 10^{17}$ Hz which means that $\rho = 2.8 \cdot 10^{-3}$ pc and NDIM=184.

The transport of relativistic electrons with the length of the step equal to the relativistic electron gyro-radius is called Bohm diffusion Bohm et al. (1949) and the diffusion coefficient will be frequency (energy) dependent. The assumption of the Bohm diffusion allows to fix a one-to-one correspondence between frequency (energy) and length of the step of the random walk.

2.4. The data on SN1006

The diameter of the known remnants spans the range from 3 pc to 60 pc and attention is fixed on SN 1006 and its possible diameter of 12.7 pc, see Strom (1988). Information on the thickness of emitting layers is contained in a recent study by Bamba et al. (2003) which analyses Chandra observations (i.e., synchrotron X-rays) from SN 1006. The observations found that sources of non-thermal radiation are likely to be thin sheets with a thickness of about 0.04 pc upstream and 0.2 pc

downstream of the surface of maximum emission, which coincide with the locations of Balmer-line optical emission, see Ellison et al. (1994). The values of W_u and W_d are now introduced in the same way as equation (1) by Bamba et al. (2003) (the values of x after which the X-ray intensity is smaller by a factor e in the upstream and downstream directions respectively)

$$f(x) = \begin{cases} A \exp -\left|\frac{x_0-x}{W_u}\right| & \text{upstream} \\ A \exp -\left|\frac{x_0-x}{W_d}\right| & \text{downstream} . \end{cases} \quad (10)$$

Here A is the amplitude of the cut and x_0 is the position of maximum emission. Observation of the six filaments, see Bamba et al. (2003), gives the following averaged values in the case of non-thermal emission: $W_u=0.04$ pc and $W_d=0.2$ pc. These observations allow us to build the intensity of an averaged theoretical X-filament, Figure 1.

For reasons that will be clarified in Sect. 3 we introduce $b=\frac{SNR \text{ diameter}}{2} = 6.35$ pc, $a=b-W_d=6.15$ pc and $c=b+W_u=6.39$ pc. Another interesting parameter is the *side* of the cubical box situated between the internal absorbing sphere of radius a and the external absorbing sphere of radius c ; this small box will be useful to simulate the transport of particles from the shock region toward the upstream and downstream regions.

The thickness of the layer, ΔR , is $\frac{SNR \text{ radius}}{12}$ according to McCray (1987) and allows us to deduce the theoretical value *side*=0.52 pc. Another useful cubical box includes all the SNR and has, for example, *side*_{SNR}=18.37 pc; this will be called the great box. The value here adopted in the magnetic field, $H_4=0.15$, is similar to $H=10\mu$ Gauss of Bamba et al. (2003); Dyer et al. (2004) quote a smaller value, $H=4\mu$ Gauss. The data presented here plus the spectral index on non thermal X-radiation (see Bamba et al. (2003)) plus the ratio of flux in the ring/center regions, Dyer et al. (2004), are reported in Table 1 together the meaning of the symbols.

One should remember that the profiles of non-thermal X-ray emission in Bamba et al. (2003) are found in another diffusion model. They are extracted from the total X-ray flux when the thermal component is not negligible. Suggestions for a new diffusion model will be presented in Sect. 3 but up to that section the exponential profiles in Bamba et al. (2003) will be the observational reference. Roughly speaking we can say that given two decreasing profiles of intensity, downstream and upstream in respect to the position of the advancing shock, the exponential fits can represent a first approximate description of a more complex behaviour of the intensity, see Sect. 3.

3. Mathematical diffusion

Once the concentration, C , the energy per electron or nucleon, ϵ_k , the spatial coordinates, \mathbf{r} , the diffusion tensor $\widehat{D}(r, \epsilon_k)$ are introduced and the losses are neglected the general diffusion transport equation for a specie (electrons or nucleons) is, see for example equation (3.1) in Berezhinskii et al. (1990),

$$\frac{\partial C}{\partial t} = \nabla \cdot (\widehat{D}(r, \epsilon_k)) \nabla C . \quad (11)$$

In general $\widehat{D}(r, \epsilon_k)$ is variable both for the standard "thermal" diffusion and for the

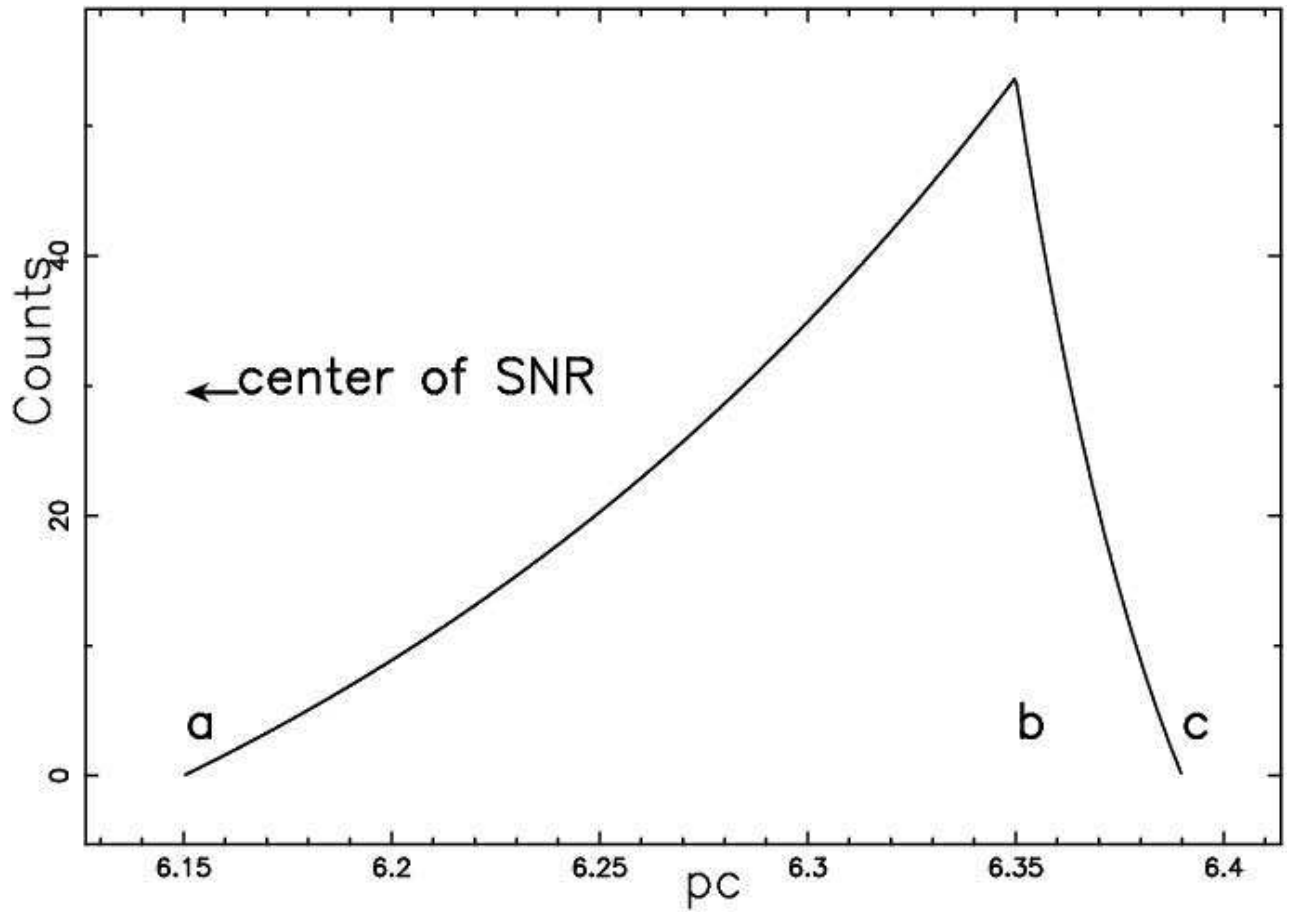


Figure 1: Profile of intensity of a non-thermal filament in the SN 1006 northeast shell in the X-band inserted in the small box. Adapted from Figure 4 in Bamba et al. (2003) .

Table 1: The data on SN 1006

<i>symbol</i>	<i>meaning</i>	<i>value</i>
<i>a</i>	<i>radius of the internal absorbing sphere</i>	6.15 <i>pc</i>
<i>b</i>	<i>radius of the shock</i>	6.35 <i>pc</i>
<i>c</i>	<i>radius of the external absorbing sphere</i>	6.39 <i>pc</i>
<i>side</i>	<i>theoretical distance between internal and external absorbing sphere</i>	0.52 <i>pc</i>
<i>side_{SNR}</i>	<i>side of a big box including the SNR</i>	18.37 <i>pc</i>
<i>H₄</i>	<i>magnetic field in 10⁻⁴ Gauss</i>	0.15
<i>u_s</i>	<i>shock velocity in km s⁻¹</i>	2600
Γ	<i>spectral index(2.0 – 10.0keV)</i>	(2.1 – 2.4)
$\frac{NT \text{ flux limb}}{NT \text{ flux center}}$	<i>ratio of X – NT flux at limb on X – NT flux at center</i>	(5.4 – 10.8)

Bohm one. Here we will concentrate on the case of constant energy (or negligible losses) that in our astrophysical case means a given frequency of observation , see formula (53). Therefore $\widehat{D}(r, \epsilon_k)$ is independent from the spatial coordinates and transforms in D that is now constant; of course the given energy/frequency of astrophysical interest should always be specified because the mean free path (i.e. Bohm diffusion) changes. The diffusion equation (11) becomes the Fick' s second equation , see for example Berg (1993) , and it's expression is different according to the chosen dimension. In three dimensions it is

$$\frac{\partial C}{\partial t} = D \nabla^2 C \quad , \quad (12)$$

in one dimension it is

$$\frac{\partial C}{\partial t} = D \frac{\partial^2 C}{\partial x^2} \quad . \quad (13)$$

In one dimension and in the presence of a drift velocity along the x-direction *u* is

$$\frac{\partial C}{\partial t} = D \frac{\partial^2 C}{\partial x^2} - \vec{u} \frac{\partial C}{\partial x} \quad . \quad (14)$$

The hypothesis of the steady state allows us to deduce simple solutions for the concentration in 3D , 1D and 1D with drift and for the spectral index.

The physical justification that allows to set the concentration equal to zero at a given distance from the source is reported in Sect. 4.2.3 and Sect. 6.3.

The solutions for the diffusion equation can also be obtained with the usual methods of eigenfunction expansion (see Gustafson (1980)

and Morse & Feshbachm (1953)) and they are cosine series whose coefficients decay exponentially; they can be deduced from formula (25) of Ferraro & Zaninetti (2004) upon inserting the dimension d .

3.1. 3D case

Figure 2 shows a spherical shell source of radius b between a spherical absorber of radius a and a spherical absorber of radius c .

The concentration raises from 0 at $r=a$ to a maximum value C_m at $r=b$ and then falls again to 0 at $r=c$. The solution of equation (12) in presence of steady state is

$$C(r) = A + \frac{B}{r} \quad , \quad (15)$$

where A and B are determined by the boundary conditions ,

$$C_{ab}(r) = C_m \left(1 - \frac{a}{r}\right) \left(1 - \frac{a}{b}\right)^{-1} \quad a \leq r \leq b \quad , \quad (16)$$

and

$$C_{bc}(r) = C_m \left(\frac{c}{r} - 1\right) \left(\frac{c}{b} - 1\right)^{-1} \quad b \leq r \leq c \quad . \quad (17)$$

These solutions can be found in Berg (1993) or in Crank 1979 . Thus a comparison can be made between the observed and the theoretical spherical solution , see Figure 3.

3.2. 1D case

The 1D solution of the concentration is the same as the diffusion through a plane sheet. If we have a point source at distance b between a point absorber of distance a and a point absorber of distance c , the general solution of equation (13) as a function of the variable x that denotes the distance in presence of steady state is

$$C(x) = A + Bx \quad . \quad (18)$$

The boundary condition gives

$$C(x) = C_m \frac{x-a}{b-a} \quad a \leq x \leq b \quad , \quad (19)$$

and

$$C(x) = C_m \frac{x-c}{b-c} \quad b \leq x \leq c \quad . \quad (20)$$

Figure 4 reports the observed X-profiles as well as the profiles of the 1D concentration as given by the diffusion from a plane.

3.3. 1D case with drift

Also here a point source at distance b between a point absorber at distance a and a point absorber at distance c are considered. The general solution of equation (14) in presence of steady state is

$$C(x) = A + B e^{\frac{x}{D}} \quad . \quad (21)$$

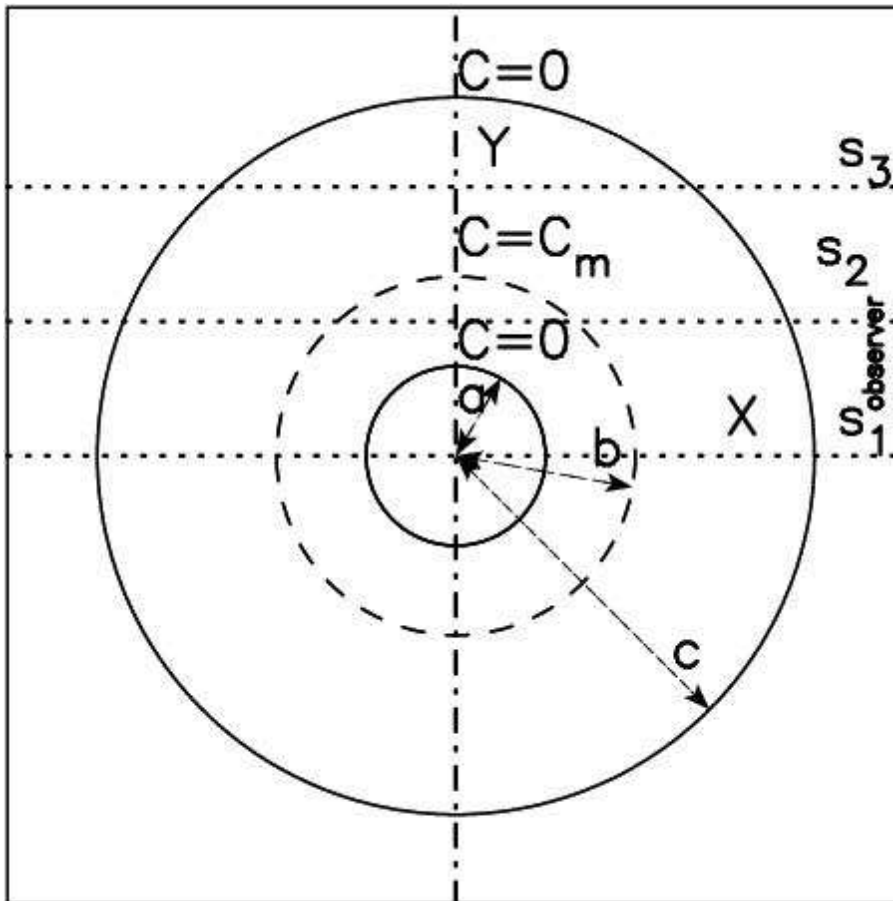


Figure 2: The spherical source inserted in the great box is represented through a dashed line, and the two absorbing boundaries with a full line. The observer is situated along the x direction, and three lines of sight are indicated. Adapted from Figure 3.1 by Berg (1993) .

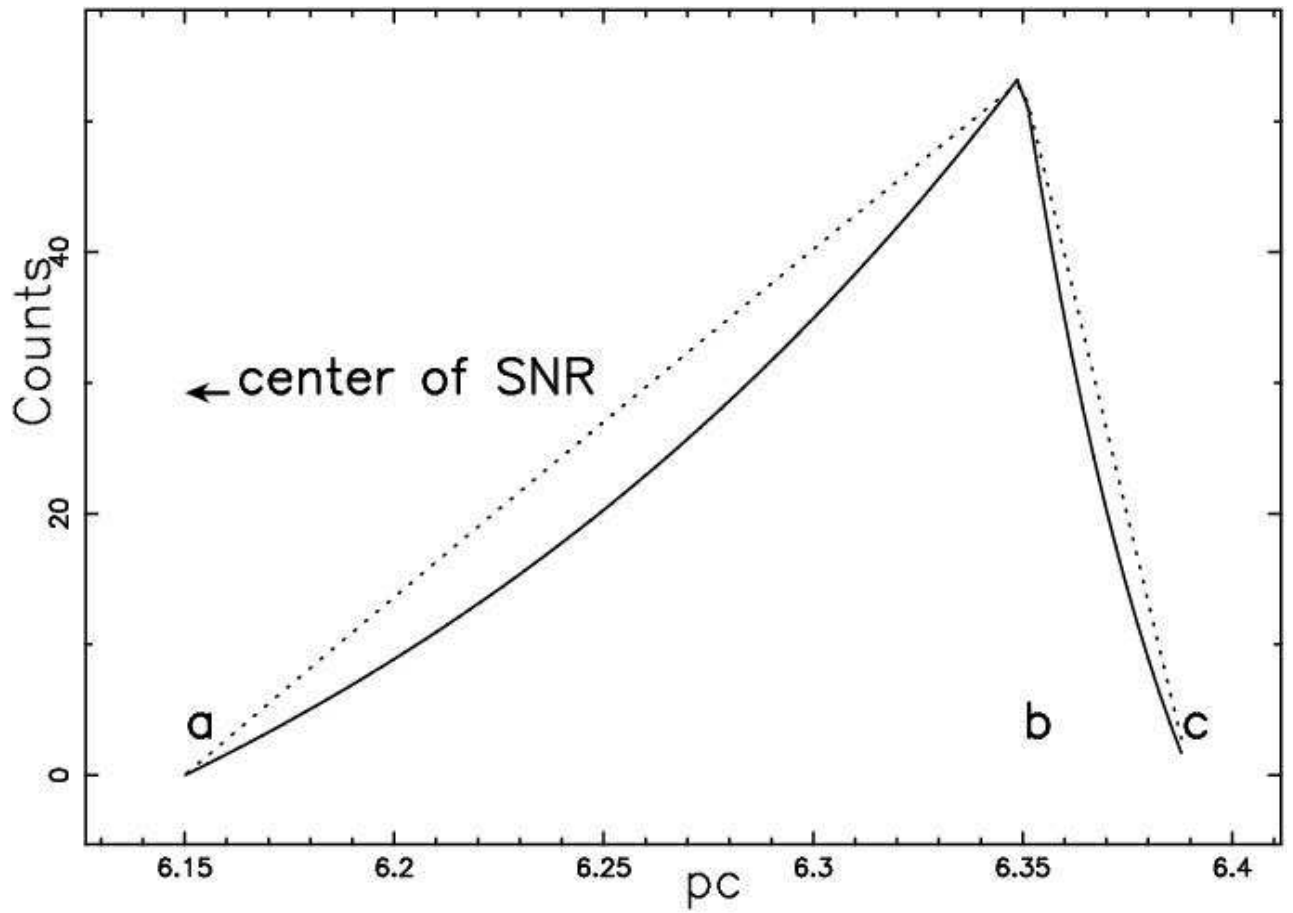


Figure 3: Observed profile of the non-thermal X filament in SN 1006 (full line) and spherical solution of the 3D concentration (dotted line) inserted in the small box. Parameters as in Table 1.

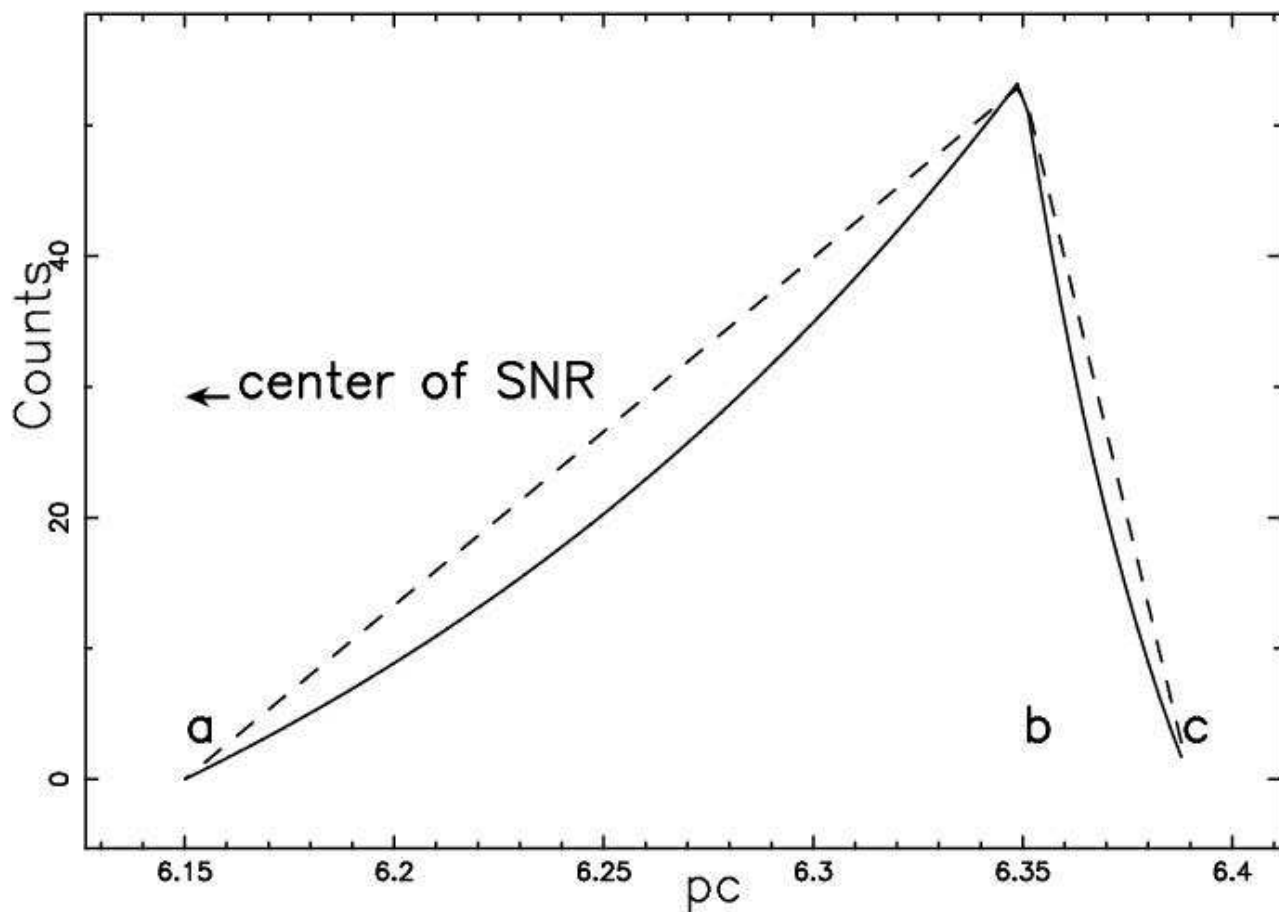


Figure 4: Observed profile of the non-thermal X filament in SN 1006 (full line) and 1D solution of the concentration (dashed line) inserted in the small box. Parameters as in Table 1.

The advection velocity here considered is the downstream velocity of the shock that has direction toward the center of the SNR , conversely the triplet a, b, c , determines a positive direction toward the advancing shock in the laboratory frame. In our application u and x have opposite directions and therefore u is negative ; the solution is

$$C(x) = A + Be^{-\frac{u}{D}x} \quad , \quad (22)$$

now the velocity u is a scalar. The boundary conditions gives

$$C(x) = \frac{C_m}{e^{-\frac{u}{D}b} - e^{-\frac{u}{D}a}} (e^{-\frac{u}{D}x} - e^{-\frac{u}{D}a}) \quad a \leq x \leq b \quad \text{downstream side} \quad , \quad (23)$$

and

$$C(x) = \frac{C_m}{e^{-\frac{u}{D}b} - e^{-\frac{u}{D}c}} (e^{-\frac{u}{D}x} - e^{-\frac{u}{D}c}) \quad b \leq x \leq c \quad \text{upstream side} \quad . \quad (24)$$

Figure 5 reports the observed X-profiles of intensity as well as the asymmetric profiles of 1D concentration as given by the mathematical diffusion from a plane in the presence of drift.

3.4. Variable spectral index in 1D

The diffusion loss equation for relativistic electrons is usually solved by neglecting the spatial diffusion. The opposite can be done by neglecting the energy losses and exploring how the variations in the absorbing boundaries influence the spectral index. Up to now the more interesting result on the prediction of the spectral index resulting from particle acceleration in shocks , i.e. SNR or Super-bubble , is due to Bell (1978a) , Bell (1978b) and Longair (1994) . The predicted differential energy spectrum of the high energy electrons is

$$C(E)dE \propto E^{-2}dE \quad . \quad (25)$$

But this is the spectral index expected where the electrons are accelerated and due to the spatial diffusion the spectral index changes.

Let us consider two energies E_1 and E_2 ($E_2 > E_1$) with two corresponding numbers of electrons C_1 and C_2 ($C_1 > C_2$) : for example with $E_2/E_1 = 10$, $C_1/C_2 = 100$.

In the framework of the 1D diffusion, the spectral index Γ of the energy will vary along the distance from the injection point according to the following formula:

$$\Gamma = \text{Log}_{10} \frac{C_1}{C_2} \quad . \quad (26)$$

In order to allow the spatial index to vary, it is enough to modify the absorbing distances of the two populations of electrons , $a_1 = a$ and $a_2 > a_1$. This effect is reported in Figure 6 where variation of the spectral index cover the observed range in the X-region , see Table 1.

4. The physics of the diffusion

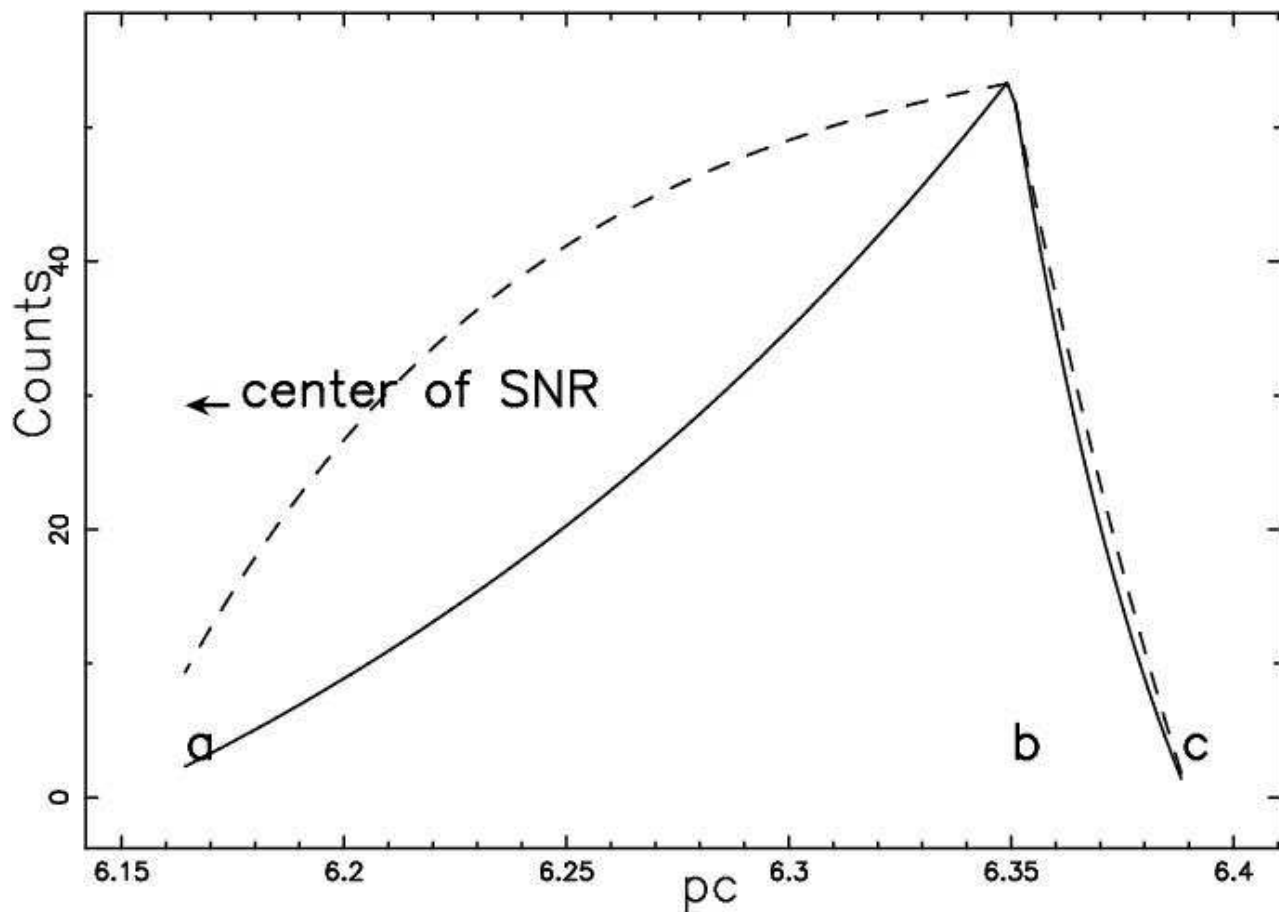


Figure 5: Observed profile of the intensity of non-thermal X filament in SN 1006 (full line) and 1D solution of concentration in the presence of drift, $\frac{u}{D} = 12.2 \text{ pc}^{-1}$ (dotted line), see formula (69) inserted in the small box. Parameters as in Table 1.

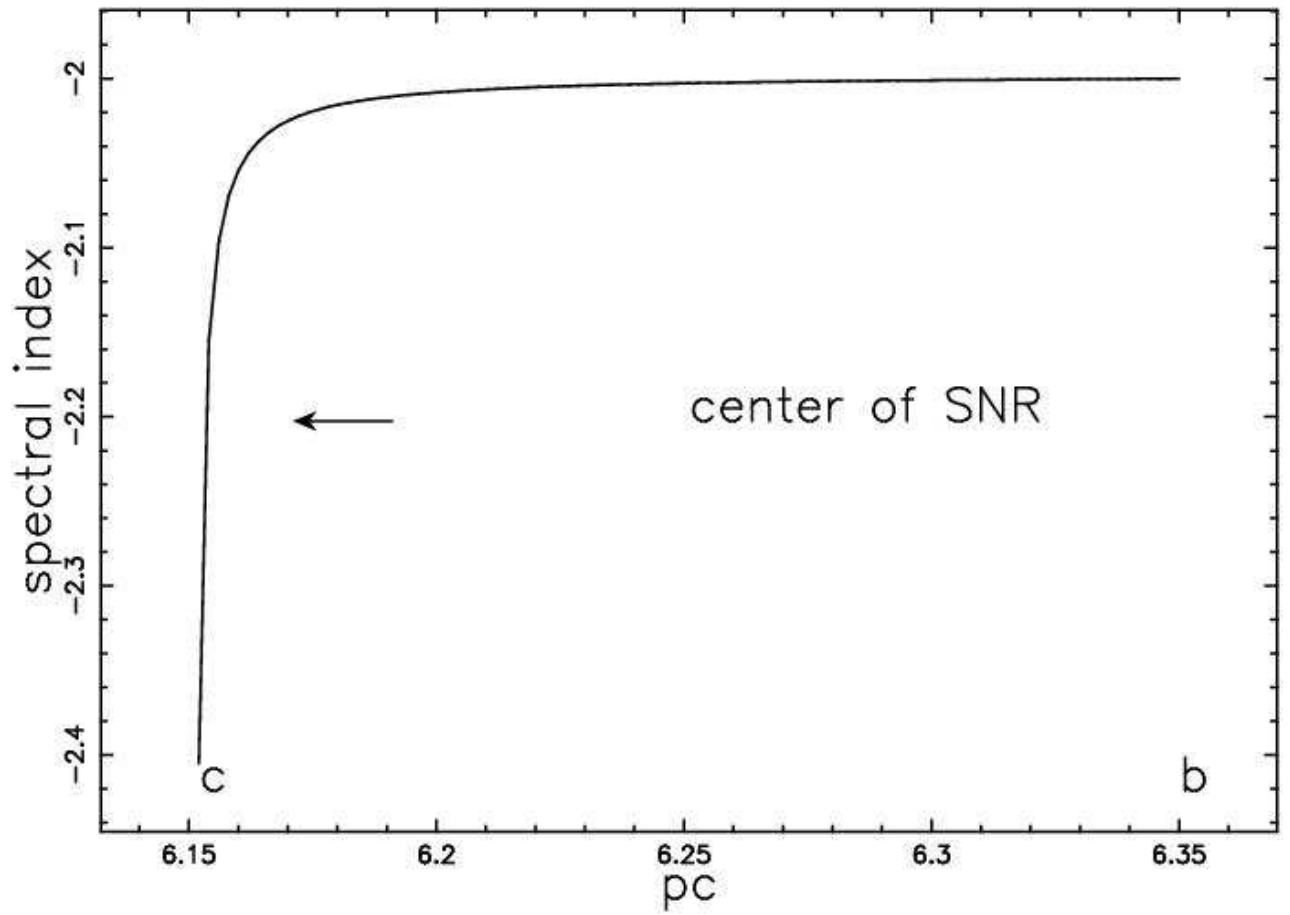


Figure 6: Behaviour of the spectral index as a function of the distance from injection point b in the downstream region of SN1006 ; $a_1 = a$, $a_2 = 1.0002 a_1$ and other parameters as in Table 1.

The reliability of the stationary state, evaluations on the residence times and the influence of synchrotron losses on the diffusion are now analysed in the light of Monte Carlo diffusion on a discrete 1D lattice. In the following, NDIM indicates the number of grid points and NPART the number of particles with different patterns.

4.1. Stationary state

It is important to stress that our simulations involving the 1D or 3D random walk cover the stationary state. Suppose, for example, that an electron reaches the boundaries (one of the two absorbing boundaries) after n steps. The visitation/concentration grid and the energy state are also marked for the previous $(n-1)$, $(n-2)$...1 steps. This means that the $(n-1)$ step was due to the electron emitted one unit of time later than that characterised by n step, the $(n-2)$ step was due to the electron emitted two units of time later than that characterised by n step and so on .

This procedure can be replicated for all the n steps ; this is equivalent to saying that $\frac{dN}{dt} = 0$ or that we are treating *the stationary state*.

We now calculate the time scales that the electrons spend inside the simulation box in order to test "The stationary state hypothesis". The time elapsed from the injection in the central point is:

$$t_{rw} = N_{step}\delta(pc)2/c = N_{step}\delta(pc) 6.52 \text{ yr} \quad , \quad (27)$$

where N_{step} is the number of steps before reaching one of the two boundaries and the time of crossing the distance δ is doubled according to formula (91). The number of steps necessary to reach the boundaries depends on the numbers NDIM and NPART : its distribution is characterised by a maximum value N_{step}^{max} which is extracted from the simulation . The inequality characterising the "The stationary state hypothesis" is :

$$t_{exp} > t_{rw} \quad , \quad (28)$$

where t_{exp} is defined in .

The stationary state hypothesis can be checked through a numerical and analytical argument. These two arguments depend fully on the choice of diffusion , basically $\overline{R^2} \propto N$; other choices of D can produce different results.

Here we have assumed that the acceleration times are smaller than the time of losses or expansion or in other words the electrons are accelerated in a smaller region in respect to that one in which they diffuse. A detailed discussion of the concept of the steady state when acceleration and cooling times are comparable can be found in Drury (1983) .

4.1.1. Numerical estimate

In every simulation the following inequality should be checked:

$$N_{step}^{max} < \frac{2.5 \times t_{SNR}}{6.52 \times \delta(pc)} \quad . \quad (29)$$

4.1.2. Analytical estimate

A simple analytical estimate for the residence time of a particle diffusing out from a box of dimension L is presented. The typical diffusing time τ is

$$\tau = \frac{\overline{R^2}}{2dD} \quad , \quad (30)$$

where $\overline{R^2(t)}$ is the mean square displacement (see Gould & Tobochnik (1988) , equation (8.38)) , $D = \frac{1}{2} \frac{c}{\delta} \delta$ is the diffusion coefficient and d is the dimension , in our case 1. On assuming that $R = L/2$ we obtain

$$\tau = \frac{1}{2} \frac{L}{\delta} \frac{L}{c} \quad , \quad (31)$$

where the mean free path has been replaced by the length of the step δ . The steady state hypothesis is represented by

$$\tau \ll t_{exp} = \frac{5}{2} t_{SNR} \quad , \quad (32)$$

which corresponds to

$$NDIM \ll t_{exp} = 5 t_{SNR} \frac{c}{L} \quad , \quad (33)$$

once $\frac{L}{\delta}$ has been replaced by $NDIM$. Assuming $L = \frac{R_{SNR}}{12}$, the inequality becomes

$$NDIM \ll 60 t_{SNR} \frac{c}{R_{SNR}} \quad . \quad (34)$$

The radius of a SNR is known to be $R_{SNR} \propto t_{SNR}^{2/5}$

$$V_{SNR} = \frac{2}{5} \frac{R_{SNR}}{t_{SNR}} \quad , \quad (35)$$

and the inequality becomes

$$NDIM \ll 24 \frac{c}{V_{SNR}} \quad , \quad (36)$$

and given $\frac{c}{V_{SNR}} \approx 100$

$$NDIM \ll 2400 \quad . \quad (37)$$

4.2. Residence time

The existence of the random walk modifies the canonical formula that allows us to compute the distance over which a relativistic electron has damped its energy . An electron that loses its energy due to radiation damping has a lifetime τ_r ,

$$\tau_r \approx \frac{E}{P_r} \approx 500 E^{-1} H^{-2} sec \quad , \quad (38)$$

where E is the energy in ergs , H the magnetic field in Gauss, and P_r the total radiated power , see Lang (1999) ,formula (1.157). The synchrotron radiative lifetime of an electron depends on pitch angle ; thus equation (38) is to be regarded as a typical value of τ_r for an approximately isotropic , highly relativistic electron population.

The energy is connected to the critical frequency, see Lang (1999) ,formula (1.154) as ,

$$\nu_c = 6.266 \times 10^{18} H E^2 \text{ Hz} \quad . \quad (39)$$

The total power radiated in frequency interval , see formula (1.160) in Lang (1999) , is given by $P(\nu) \propto F(\nu/\nu_c)$ with

$$F(\nu/\nu_c) = \int_{\nu/\nu_c}^{\infty} K_{5/3}(\eta) d\eta \quad , \quad (40)$$

where $K_{5/3}(\eta)$ is a modified Bessel function. The function $F(\nu/\nu_c)$ has a maximum at $\nu/\nu_c=0.29$ and some authors , see for example Reynolds (1998) , use this numerical relationship in order to identify the energy of the electron with the observed frequency. Is also interesting to compute the averaged frequency of emission $\bar{\nu}/\nu_c$ computed as

$$\frac{\bar{\nu}}{\nu_c} = \frac{\int_{0.1}^{10} (\nu/\nu_c) F(\nu/\nu_c)}{\int_{0.1}^{10} F(\nu/\nu_c)} = 1.29 \quad . \quad (41)$$

In the following we will use $\nu/\nu_c = 1$ that can be considered an average between the two points of view previously expressed.

Upon inserting in (38) the energy as given in (39) :

$$\tau_r = 1.251 \times 10^{12} \frac{1}{\nu^{1/2} H^{3/2}} \text{ sec} \quad . \quad (42)$$

The maximum frequency that can escape from the center of the box and the parameters for which the gyro-radius equals the length of the step are now computed.

4.2.1. Maximum frequency allowed

If a box with a side L has an electron inserted at the center, the classical time of crossing the box t_c is :

$$t_c = \frac{L}{2c} \quad . \quad (43)$$

The solution of the equation

$$\frac{\tau_r}{t_c} = 1 \quad , \quad (44)$$

gives the maximum allowed frequency , ν_c^{max}

$$\nu_c^{max} = 5.962 \times 10^{20} \frac{1}{L_{pc}^2 H_{-4}^3} \text{ Hz} \quad , \quad (45)$$

where L_{pc} is the side in pc and H_{-4} the magnetic field in 10^{-4} Gauss units . Upon inserting the typical parameters of SN 1006 , reported in Table 1:

$$\nu_c^{max} = 6.490 \times 10^{23} \text{ Hz} \quad . \quad (46)$$

For greater frequencies the electron cannot escape from the box when the classical treatment is adopted . The time t_{rw} necessary to escape from the box in the presence of a random walk is

$$t_{rw} = \frac{L^2}{4\delta v_{tr}} \quad . \quad (47)$$

The equation to be solved is now

$$\frac{\tau_r}{t_{rw}} = 1 \quad . \quad (48)$$

By imposing $v_{tr} = \frac{c}{c_f}$, where c_f is a parameter greater than one, the maximum frequency $\nu_{c,rw}^{max}$ carried by the electron is

$$\nu_{c,rw}^{max} = \nu_c^{max} \times \left(\frac{2}{c_f \text{NDIM}} \right)^2 \quad . \quad (49)$$

The relativistic electrons move at velocity near to that of the light but the trajectory is not rectilinear. The parameter c_f averages the irregularities and fixes the transport velocity once the length and the direction of the step are fixed. The presence of the random walk produces a decrease in the maximum frequency that can be carried by the electron . For example, with $\nu_{c,rw}^{max} = 4.0 \cdot 10^{17} \text{ Hz}$, and assuming $c_f=2$ the maximum value allowed for NDIM is 1273; for bigger values of NDIM the X-ray emission cannot be sustained.

4.2.2. Damping length and gyro-radius

The length travelled by the electron L_{rw} before being damped is

$$L_{rw}^2 = 2dDt_{rw} \quad . \quad (50)$$

On replacing t_{rw} with it's physical value we obtain the damping length

$$L_{rw} = 110.312 \left(\frac{L_{pc}}{c_f \text{NDIM}} \right)^{1/2} \times \left(\frac{1}{H^{3/4} \nu_c^{1/4}} \right) pc \quad . \quad (51)$$

The electron gyro-radius , see Lang (1999) , formula (1.153), is

$$\rho \approx 2 \times 10^9 EH^{-1} cm \quad , \quad (52)$$

with energy in ergs and H in Gauss . It can be expressed in pc by introducing the critical frequency (in Hz) , (Bohm diffusion)

$$\rho \approx 2.67 \times 10^{-19} \frac{\nu_c^{1/2}}{H^{3/2}} pc \quad . \quad (53)$$

In order to have transport the following inequality should be satisfied

$$\rho < L_{rw} \quad . \quad (54)$$

If equation (53) is solved for ν , the following is obtained:

$$\nu < 3.197 \times 10^{27} H \left(\frac{L_{pc}}{c_f NDIM} \right)^{2/3} Hz \quad . \quad (55)$$

With the data from Sect. 4, for example, the inequality is verified: the right hand side of (55) is $6.062 \cdot 10^{20}$ Hz and the left hand side is $\nu = 4 \cdot 10^{17}$ Hz. It is also possible to test the hypothesis of random walk without appreciable synchrotron losses; expressed as an inequality is

$$L_{rw} > L_{pc} \quad . \quad (56)$$

Upon inserting the typical values of the X-region (NDIM=183 and $\nu = 4 \cdot 10^{17}$ Hz) formula (51) gives

$$0.62 > L_{pc} \quad , \quad (57)$$

and as being $L_{pc}=0.52$, the inequality is verified. In the radio region (NDIM=2 10^7 and $\nu = 30 \cdot 10^6$ Hz) the application of formula (51) gives

$$0.7 > L_{pc} \quad , \quad (58)$$

and therefore the inequality is verified.

4.2.3. Number of collisions on an unbounded lattice

The random walk in 1D on an unbounded lattice is characterised by the length of the step δ , which in our case is equalised to the value of the electron's gyro-radius ρ , and by the number of steps after which the random motion is stopped. The damping time τ_r , is given by equation (38) and the time τ_ρ , necessary to travel a distance $\delta = \rho$ at a velocity $v_{tr} = \frac{c}{c_f}$ is

$$\tau_\rho = 2.66 \times 10^{-11} \frac{\sqrt{H\nu_c c_f}}{H^2} sec \quad , \quad (59)$$

where ν_c is expressed in Hz and H in Gauss. The number of collisions made by the electron before halving it's energy is

$$N = \frac{\tau_r}{\tau_\rho} = 4.699 \times 10^{22} \frac{1}{\nu_c c_f} \quad . \quad (60)$$

Table 2 reports the set of parameters after which the profile of the concentration in the asymmetric 1D random walk is similar to the observed one. The number of collisions before to damp the relativistic electron is independent from the magnetic field but depends from c_f the factor that fixes the transport velocity and ν_c , the frequency of emission. Is also possible to compute the mean square displacement $\overline{R^2(t)}$ as given by equation (30) corresponding to the damping time τ_r

$$\overline{R^2(\tau_r)} = 3.15 \times 10^{-15} \frac{1}{H^3 c_f} pc^2 \quad . \quad (61)$$

Table 2: The physical data on asymmetric 1D random walk

<i>symbol</i>	<i>meaning</i>	<i>value</i>
H_{-4}	<i>magnetic field in 10^{-4} units</i>	1.2
ρ	<i>electron's gyro – radius</i>	$1.24 \cdot 10^{-4} pc$
ν_c	<i>critical frequency in X – region</i>	$4 \cdot 10^{17} Hz$
N	<i>number of collisions</i>	58744

Is interesting to point out that the mean square displacement is independent from the chosen energy/frequency (framework of the Bohm diffusion) and therefore the observed profiles should be independent from the chosen type of astronomy. This independence from the band of observation can explain Figure 4 of Dyer et al. (2004) where there are minimum differences between radio and x profiles in the image of SN1006.

The assumption of the mathematical diffusion that sets the concentration equal to zero at a given distance from the plane where the diffusing substance is introduced , is justified by the physical effect here described.

5. Montecarlo diffusion

A numerical simulation is now performed by implementing the asymmetric random walk of a charged particle on a 1D regular network consisting of a lattice with $NDIM$ grid points embedded on a length $side(pc)$; the conversion between the unit-length and physical dimension of one step is the factor $\frac{side(pc)}{(NDIM-1)}$. The analysis is divided into random walks with absorbing boundaries and random walks on an infinite or unbounded lattice.

5.1. Absorbing boundaries

The rules adopted in implementing the 1D asymmetric random walk with injection in the middle of the grid are :

1. The first of the NPART electrons is chosen.
2. The random walk of an electron starts in the middle of the grid. The probabilities of having one step are p_1 in the negative direction (upstream) $p_1 = \frac{1}{2} - asym \times \frac{1}{2}$, and p_2 in the positive direction (downstream) , $p_2 = \frac{1}{2} + asym \times \frac{1}{2}$.
3. When the electron reaches one of the two absorbing points , the motion starts another time from (2) with a different diffusing pattern.
4. The number of visits is recorded on \mathcal{M} , a one-dimensional grid.
5. The random walk terminates when all the NPART electrons are processed.

6. For the sake of normalisation the one-dimensional visitation/concentration grid \mathcal{M} is divided by NPART.

These transition probabilities can be considered the 1D counterpart of the 2D formula (4.5) in Ferraro & Zaninetti (2001) . The introduction of the asymmetry in the probability means that it is possible to simulate diffusion and convection.

There is a systematic change of the average particle position along the x-direction:

$$\langle dx \rangle = asym \delta \quad , \quad (62)$$

per each time step. If the time step is $dt = \frac{\delta}{v_{tr}}$ and the transport velocity

$$v_{tr} = \frac{c}{c_f} \quad , \quad (63)$$

where c_f is a parameter greater than one , the convection velocity u is

$$u = \frac{asym \ c}{c_f} \quad . \quad (64)$$

The density distribution is actually determined by the ratio u/D rather than u or D separately, so using a single u and D throughout the system only means that the ratio is fixed to a constant value. Let consider a strong shock moving in the laboratory frame with velocity u_s . The post-shock speed is

$$u_p = u_s \frac{3}{4} \quad , \quad (65)$$

and the post-shock gas moves in the same direction as the shock. On introducing the index u and d , denoting respectively the upstream and the downstream region, the ratio of the Larmor-radii is

$$\frac{\rho_u}{\rho_d} = \frac{H_d}{H_u} = 4 \quad , \quad (66)$$

, see equation (9.8b) and equation (9.12) in McKee (1987) .

Let now consider a frame in which the shock is at rest . The downstream velocity , u_{ds} , is

$$u_{ds} = \frac{3}{4}u_s - u_s = -\frac{1}{4}u_s \quad . \quad (67)$$

The downstream velocity is negative and is 1/4 of the shock velocity; of course if we take an x-axis with positive direction toward the center of SNR this velocity is positive.

Thus, using a single value for both u (the advection velocity) and D (the diffusion coefficient) may be justified, but for these values the downstream velocity $\frac{u_s}{4} = 650 \text{ km s}^{-1}$ and the downstream ρ_d (which corresponds to the magnetic field of equipartition and the largest radiative region) for δ should be used.

The expected value of $asym$ can now be easily deduced from equation (64) by inserting $u = \frac{u_s}{4}$:

$$asym = c_f * 0.0021 \quad , \quad (68)$$

and Figure 7 reports the observed X-profile as well as the profile of concentration as given by the 1D random walk with drift. A formula for the ratio $\frac{u}{D}$, where u represents the drift velocity, can be derived in the X-region

$$\frac{u}{D} = 2 \frac{u}{c} c_f \frac{NDIM}{side} = 1.525 c_f pc^{-1} . \quad (69)$$

5.2. Unbounded lattice

The procedure that describes the random walk is the same as the previous subsection except for the fact that the random walk at item (3) stops after N steps rather than when one of the two limiting boundaries is reached. Figure 8 reports the observed X-profiles as well as the profiles of concentration as given by the 1D random walk with drift according to the physics explored in Sect. 4.2.3.

6. Theory of the image

The overall behaviour of SN1006 in the X-region, see for example Dyer et al. (2004), presents a spherical symmetry with a ring enhancement and a central depression. When these effects are visualised through a cut in the flux crossing the center of the image, a characteristic "U" profile is obtained. These "U" profiles can be explained through cuts of the intensity given by the 3D mathematical diffusion while the agreement with the theoretical predictions excludes the presence of absorption.

The asymmetry in the observed flux can be simulated through the map of the field of velocity.

6.1. The mathematical image

The observed flux of the overall morphology of the SNR is presented in the form of "U" profile, see dashed line in Figure 9. The theoretical intensity can be found by solving the integral equation (6) along the x direction, see Figure 2 where three lines of sight are reported.

The concentrations to be used are formulae (16) and (17) once $r = \sqrt{x^2 + y^2}$ is imposed; these two concentrations are inserted in formula (3) which represents the transfer equation. The geometry of the phenomena fixes three different zones ($0 - a, a - b, b - c$) in the variable y ; the first piece, $I^I(y)$, is

$$\begin{aligned} I^I(y) &= \int_{\sqrt{a^2 - y^2}}^{\sqrt{b^2 - y^2}} 2C_{ab} dx + \int_{\sqrt{b^2 - y^2}}^{\sqrt{c^2 - y^2}} 2C_{bc} dx \\ &= 2 \frac{bCm \left(-\sqrt{a^2 - y^2} + a \ln \left(\sqrt{a^2 - y^2} + a \right) + \sqrt{b^2 - y^2} - a \ln \left(\sqrt{b^2 - y^2} + b \right) \right)}{b - a} \\ &\quad - 2 \frac{bCm \left(c \ln \left(\sqrt{b^2 - y^2} + b \right) - \sqrt{b^2 - y^2} - c \ln \left(\sqrt{c^2 - y^2} + c \right) + \sqrt{c^2 - y^2} \right)}{c - b} \end{aligned} \quad 0 \leq y < a . \quad (70)$$

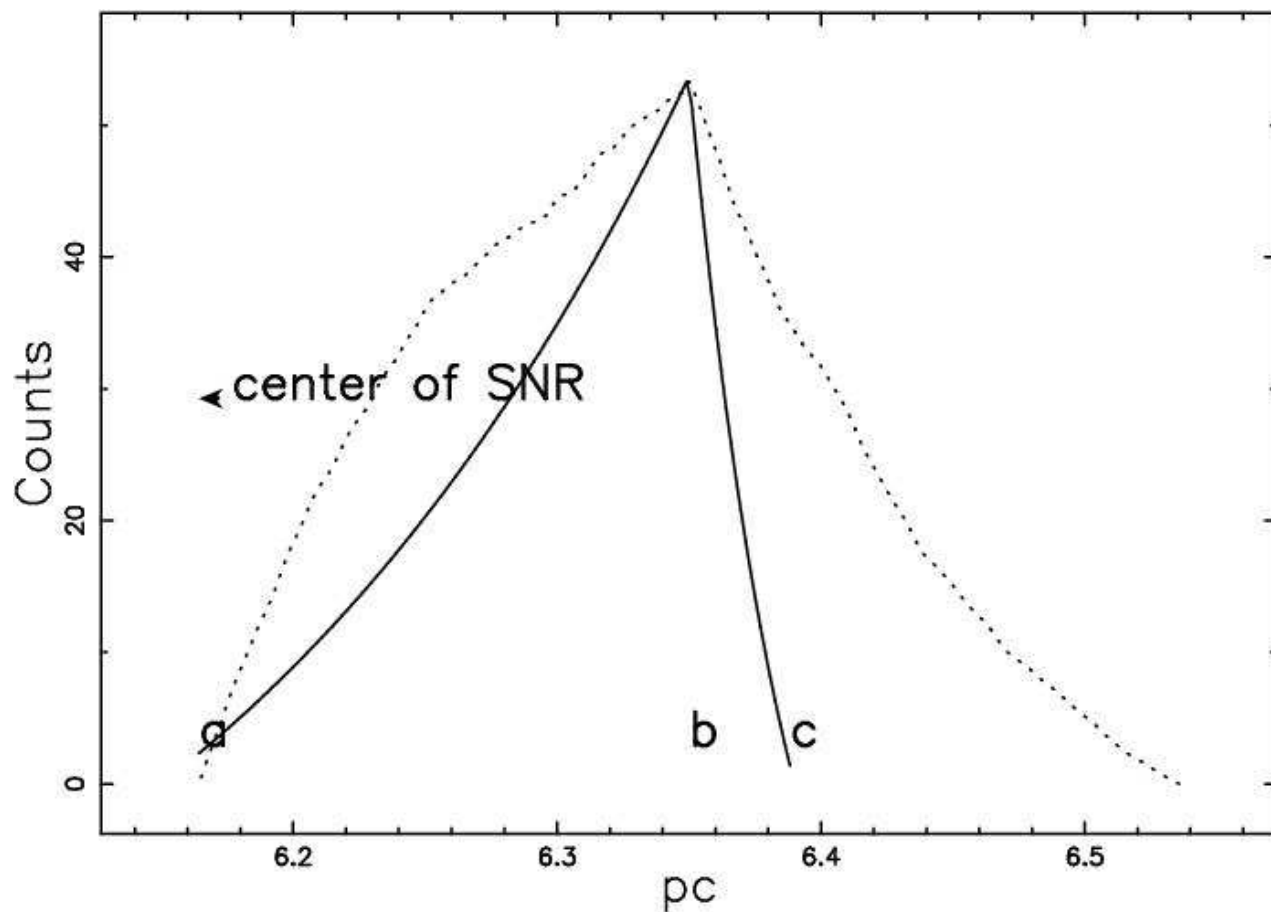


Figure 7: Observed profile of the non-thermal X filament in SN 1006 (full line) and concentration of the 1D asymmetric random walk (dotted line), NDIM=183 ,NPART=2000 , $c_f=6$ and $asym = 0.013$. Parameters as in Table 1.

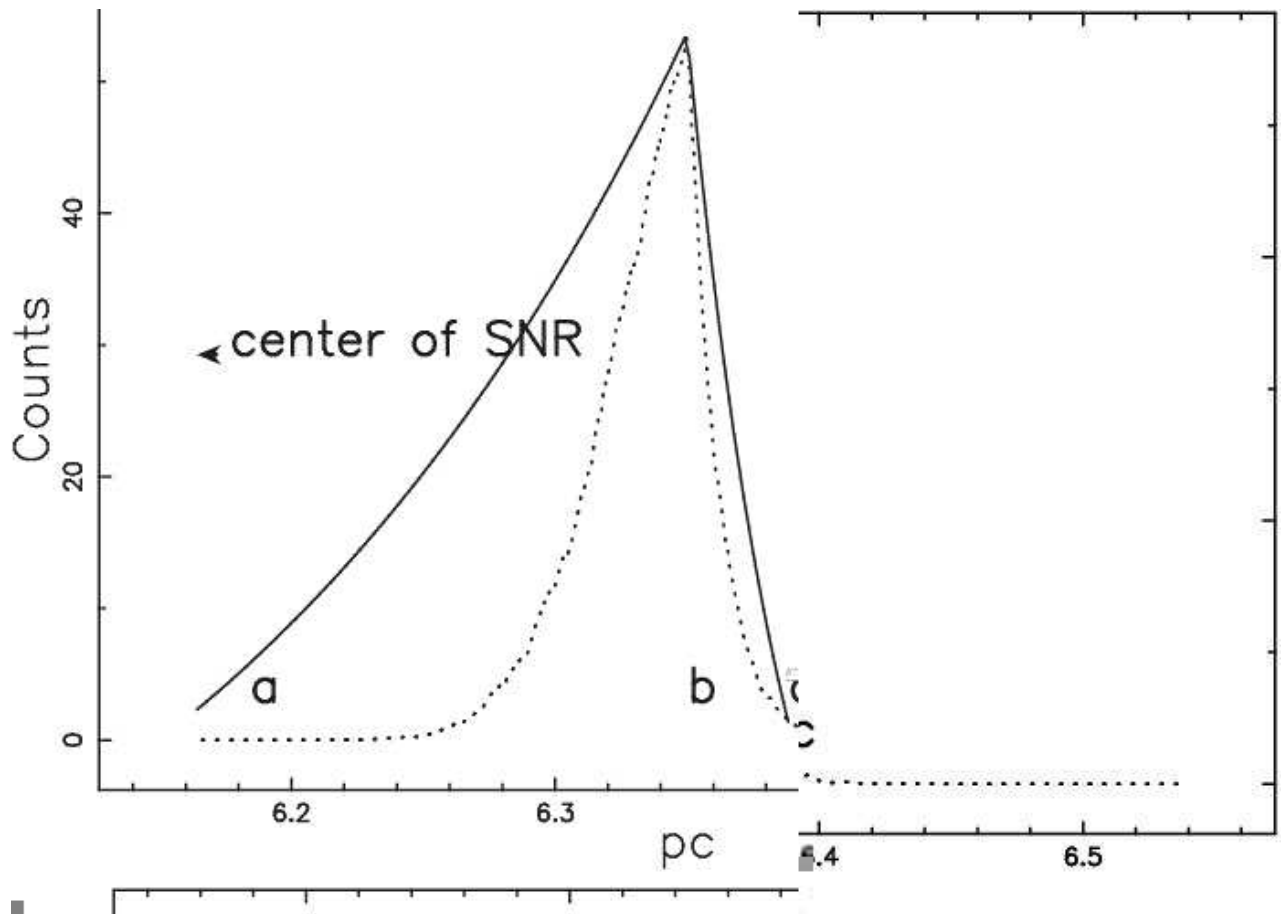


Figure 8: Observed profile of the non-thermal X filament in SN 1006 (full line) and 1D asymmetric random walk (dotted line), $NDIM=2980, NPART=2000$, $c_f=2$, $N=58744$ and $asym=0.0043$. Physical parameters as in Table 2.

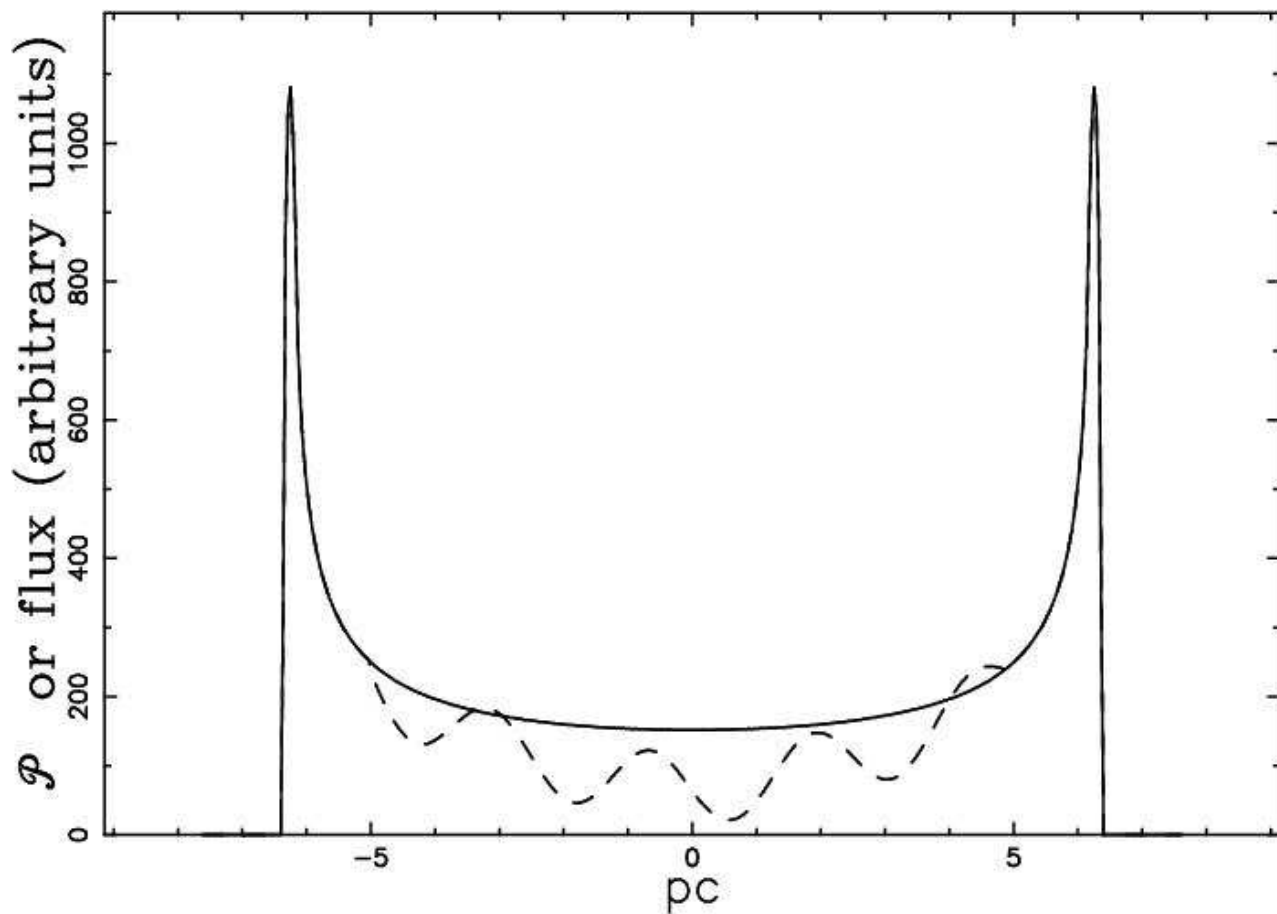


Figure 9: Cut of the mathematical intensity I crossing the center (full line) and X-ray data (dashed line) extracted from Dyer et al. (2004). Parameters as in Table 1, great box.

The second piece , $I^{II}(y)$, is

$$\begin{aligned}
I^{II}(y) &= \int_0^{\sqrt{b^2-y^2}} 2C_{ab}dx + \int_{\sqrt{b^2-y^2}}^{\sqrt{c^2-y^2}} 2C_{bc}dx \\
&= -\frac{bCm \left(-a \ln(y^2) - 2\sqrt{b^2-y^2} + 2a \ln(\sqrt{b^2-y^2} + b) \right)}{b-a} \\
&\quad - 2\frac{bCm \left(c \ln(\sqrt{b^2-y^2} + b) - \sqrt{b^2-y^2} - c \ln(\sqrt{c^2-y^2} + c) + \sqrt{c^2-y^2} \right)}{c-b}
\end{aligned}
\tag{71}$$

$a \leq y < b$.

The third piece , $I^{III}(y)$, is

$$\begin{aligned}
I^{III}(y) &= \int_0^{\sqrt{c^2-y^2}} 2C_{bc}dx \\
&= \frac{bCm \left(-c \ln(y^2) + 2c \ln(\sqrt{c^2-y^2} + c) - 2\sqrt{c^2-y^2} \right)}{c-b}
\end{aligned}
\tag{72}$$

$b \leq y < c$.

The profile of I made by the three pieces (70), (71) and (72), can then be plotted as a function of the distance from the center , see Figure 9, or like a contours , see Figure 10.

The position of the minimum of I is at $y = 0$ and the position of the maximum is situated in the region $a \leq y < b$, and more precisely at:

$$y = \frac{\sqrt{-(b-2a+c)a(ab-2bc+ac)}}{b-2a+c} .
\tag{73}$$

The ratio between the theoretical intensity at maximum , I_{max} , as given by formula (73) and at minimum ($y = 0$) is given by

$$\frac{I_{max}}{I(y=0)} = \frac{Numerator}{Denominator} ,
\tag{74}$$

where

$$\begin{aligned}
&-a \ln \left(-\frac{(ac+ab-2cb)a}{b+c-2a} \right) c + a \ln \left(-\frac{(ac+ab-2cb)a}{b+c-2a} \right) b - 2\sqrt{\frac{(c+b)(b-a)^2}{b+c-2a}} c \\
&\quad - 2a \ln \left(\sqrt{\frac{(c+b)(b-a)^2}{b+c-2a}} + b \right) b + \\
&\quad 2c \ln \left(\sqrt{\frac{(c+b)(b-a)^2}{b+c-2a}} + b \right) b + 2\sqrt{\frac{(c+b)(b-a)^2}{b+c-2a}} a
\end{aligned}$$

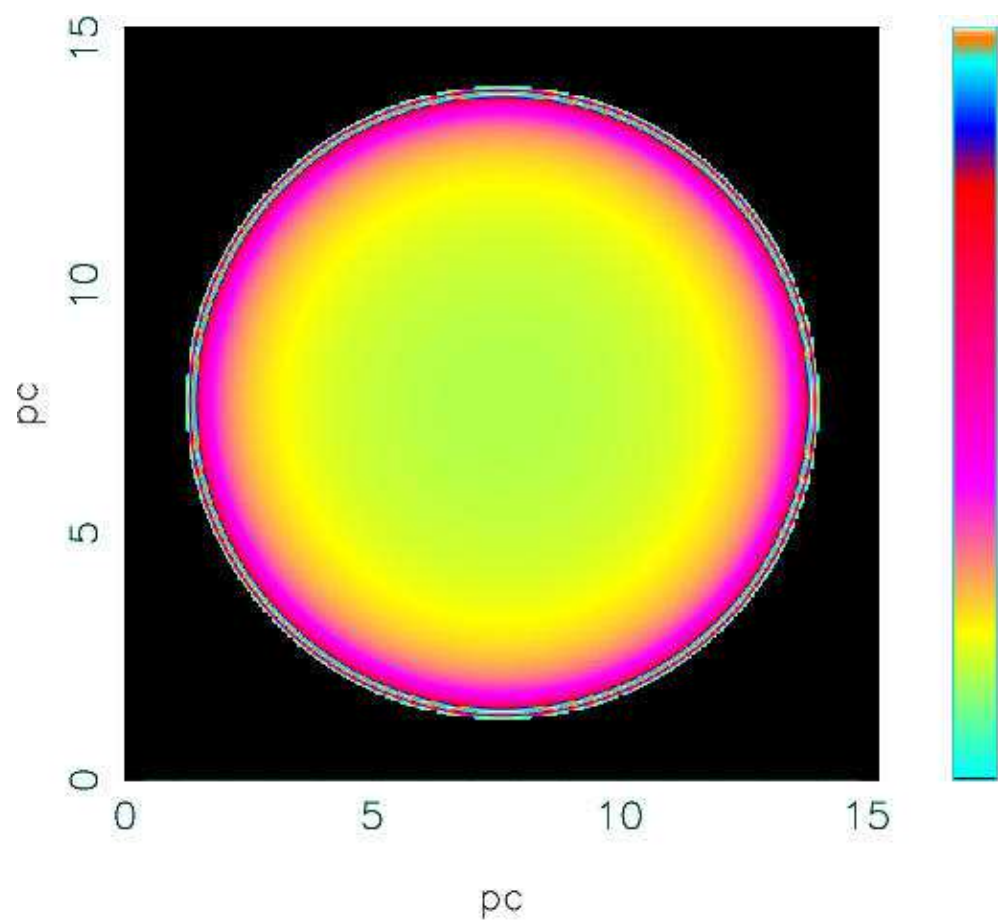


Figure 10: Contour map of I particularized to simulate the X-emissivity of SN 1006. Parameters as in Table 1, great box.

$$\begin{aligned}
& -2c \ln \left(\sqrt{\frac{(a-c)^2(c+b)}{b+c-2a}} + c \right) b + \\
& 2c \ln \left(\sqrt{\frac{(a-c)^2(c+b)}{b+c-2a}} + c \right) a + 2 \sqrt{\frac{(a-c)^2(c+b)}{b+c-2a}} b - \\
& 2 \sqrt{\frac{(a-c)^2(c+b)}{b+c-2a}} a \quad , (75)
\end{aligned}$$

and

$$\begin{aligned}
& \text{Denominator} = \\
& -2ac \ln(a) + 2ba \ln(a) - 2ba \ln(b) + 2bc \ln(b) - 2bc \ln(c) + 2ac \ln(c) \quad . (76)
\end{aligned}$$

In order to make the model more realistic the maximum value of I is normalised in order to have the same value as the flux in arbitrary units (i.e. 1080) in Figure 4 from Dyer et al. (2004) .

From the simulation reported in Figure 9 we obtain

$$\frac{I_{ring}}{I_{center}} = 7.14 \quad , (77)$$

where I_{ring} represents the maximum value of I (on the ring) and I_{center} the value at the center. The X-observations with ASCA of SN 1006 , see Figure 4 by Dyer et al. (2004) , give

$$\begin{aligned}
\frac{flux_{ring}}{flux_{center}} &= 1080/200 = 5.4 \quad \text{minimum value} \\
\frac{flux_{ring}}{flux_{center}} &= 1080/100 = 10.8 \quad \text{maximum value} \quad ,
\end{aligned}$$

here $flux_{ring}$ and $flux_{center}$ are the two fluxes in arbitrary units (200 is the maximum value of the fluxes in the central region and 100 is an approximated average value of the fluxes in the central region).

The mathematical diffusion here adopted predicts a value given $\frac{flux_{ring}}{flux_{center}} = 7.14$, which is comprised in the reasonable interval of observations given in equation (78).

It is also interesting to note that the CAP and CENTER region models (subsets of the SRESC model) adopted in Figure 4 by Dyer et al. (2004) predict ,roughly speaking, a central flux that is

$$\frac{flux_{ring}}{flux_{center}} = 1080/400 = 2.7 \quad . (78)$$

This value is three times bigger than that observed or, in other words, over-predicts the non-thermal emission at the center of the SNR.

The effect of insertion of a threshold flux , $flux_{tr}$, given by the observational techniques , is now analysed. The threshold flux can be parametrised to $flux_{max}$,

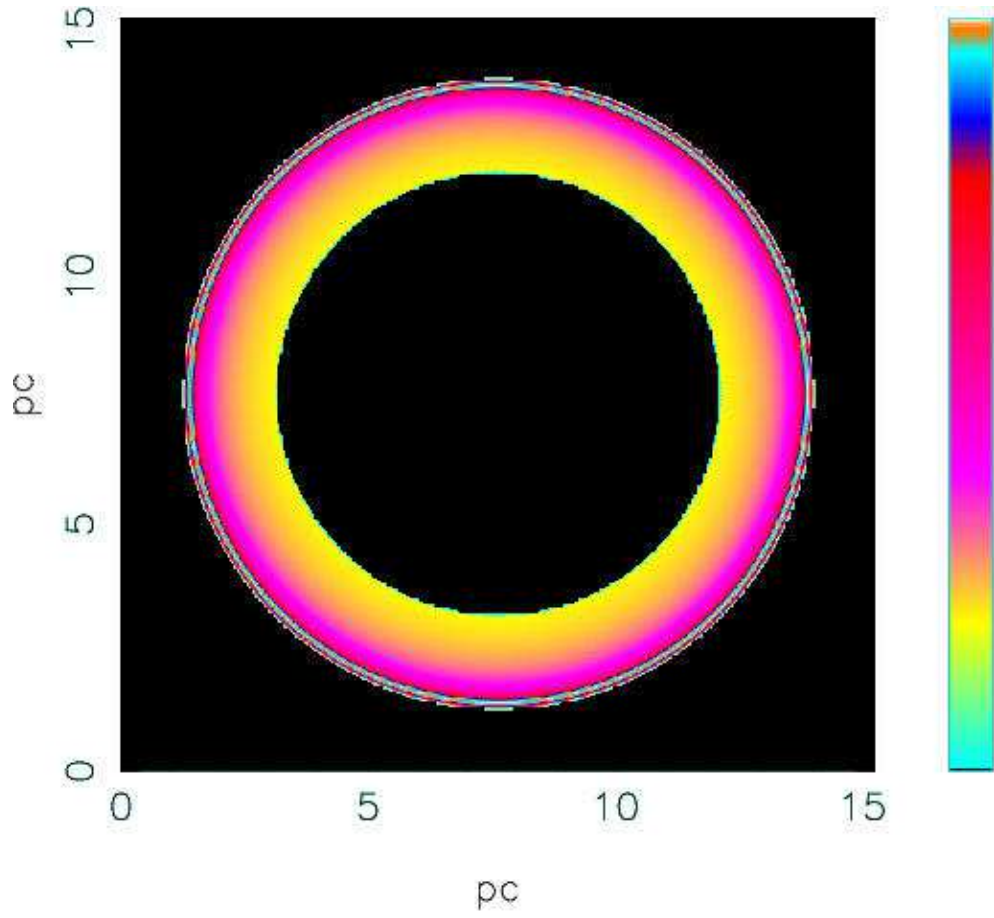


Figure 11: The same as Figure 10 but with $flux_{tr} = flux_{max}/5$

the maximum value of flux characterising the ring: a typical image with a hole is visible in Figure 11 when $flux_{tr} = flux_{max}/5$. The X-ray emission from SNR can also be presented through cuts in particular regions, see for example Figure 4 in Bamba et al. (2003), where the x-axis is reported in arc-sec and X-intensity in counts. We also particularize our results in those units, see Figure 12 where is possible to visualise the position of the maximum of the intensity that is situated between a and b . The 1D solutions of the concentration in presence of drift represented by equation (23) and (24) cannot be integrated along the line of sight in terms of elementary functions and therefore a numerical integration is performed, see dotted line in Figure 12.

6.2. The case of absorption

The effect of absorption is easily implemented by adopting formula (8) and fixing the value of K_a for which the results of the thin layer approximation are reproduced. The value of K_a is then gradually increased in order to see how the effect of the absorption modifies the "U" profiles in the cut of the intensity previously reported. This numerical experiment is visible in Figure 13 in which the transition from a "U" profile corresponding to the thin-thick case is analysed.

Due to the fact that we do not know if absorption is present or not, all the cuts are normalised in order to have the same maximum value (1080). This transition explains the anomalous value of $\frac{flux_{ring}}{flux_{center}} = 2.7$ of the CAP and CENTER codes as due to a high value adopted in the absorption's coefficient. In Figure 13 the third (dashed) line reproduces this anomalous profile. We conclude this paragraph underlying the fact that the absorption is not relevant in the X-ray frequencies.

6.3. An unbounded lattice and derivation of the magnetic field

The case of an unbounded lattice in the presence of asymmetry and the number of collisions fixed by the damping length produces profiles in the upstream and downstream region that are reported in Figure 8. These profiles can be parameterised through exponentials of the type of those reported in equation (10) characterised by W_u^{rw} and W_d^{rw} . This analytical expression of the concentration of relativistic electrons can be the base of the numerical integral along the line of sight with the algorithm outlined in equation (7). The typical behaviour of the intensity as a function of the distance from the center is reported in Figure 14.

In this case the simulation predicts a value given by $\frac{flux_{ring}}{flux_{center}} = 9.61$, which is comprised in the interval of observations given in equation (78). The magnetic field adopted in this paragraph is independent from equipartition arguments and therefore the algorithm here outlined can be considered a new way to deduce the magnetic field.

6.4. Comparison with other methods

In a study on the amplification of the magnetic field in SNR, the observed/theoretical analysis on the radial profile of RCW86 in the X-ray band, see Figure 7 in Völk et al. (2005), gives $\frac{flux_{ring}}{flux_{center}} \approx 4.5$.

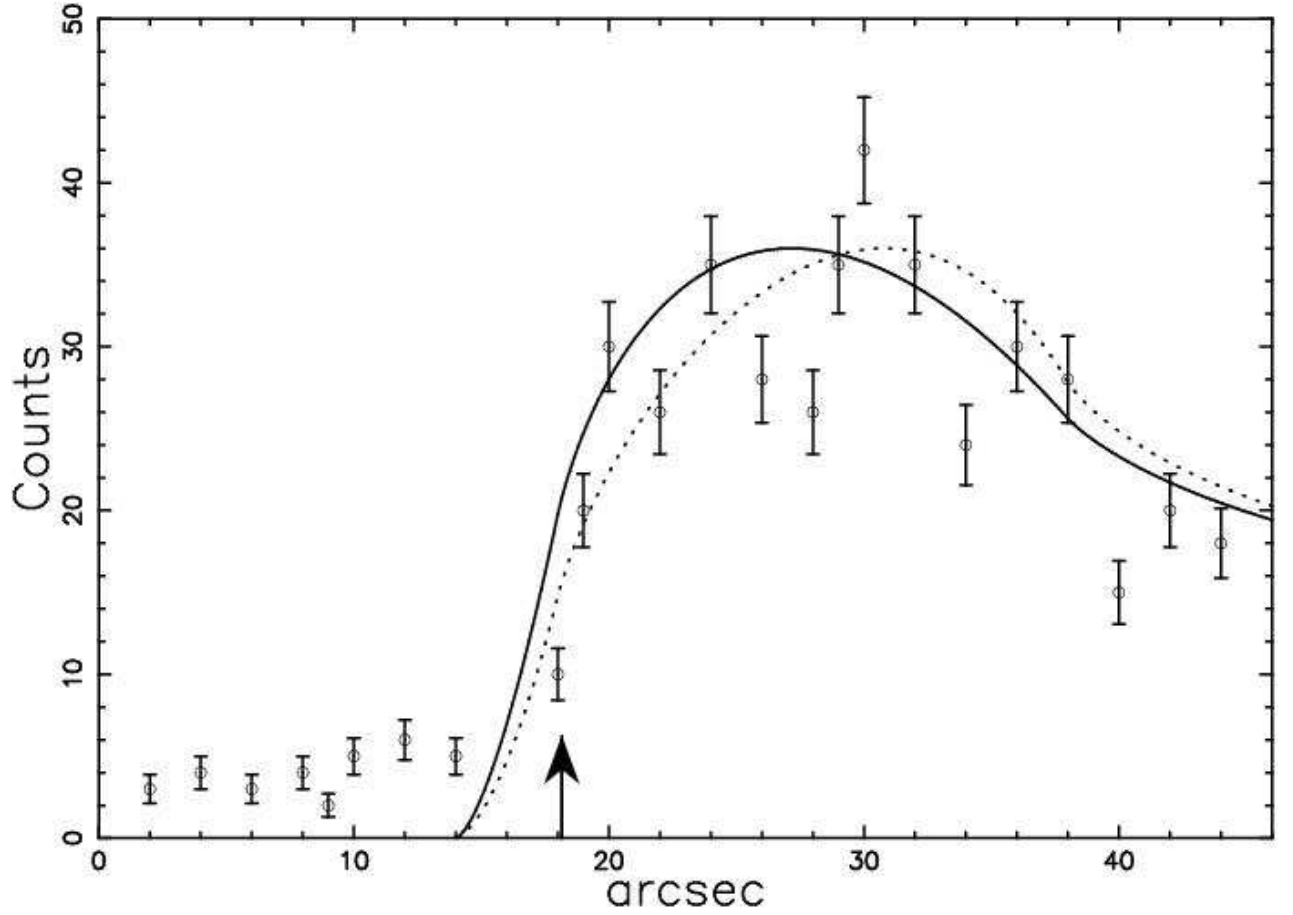


Figure 12: Cut of the mathematical intensity I , full line, that covers a spatial zoom of Figure 9 but with a different scaling. The radius of the expanding SNR, b , is marked with an arrow. The experimental data are extracted by the author from Figure 4 (panel 1a) in Bamba et al. (2003). The dotted line represents the asymmetric case with $\frac{v}{D} = 12.2 \text{ pc}^{-1}$.

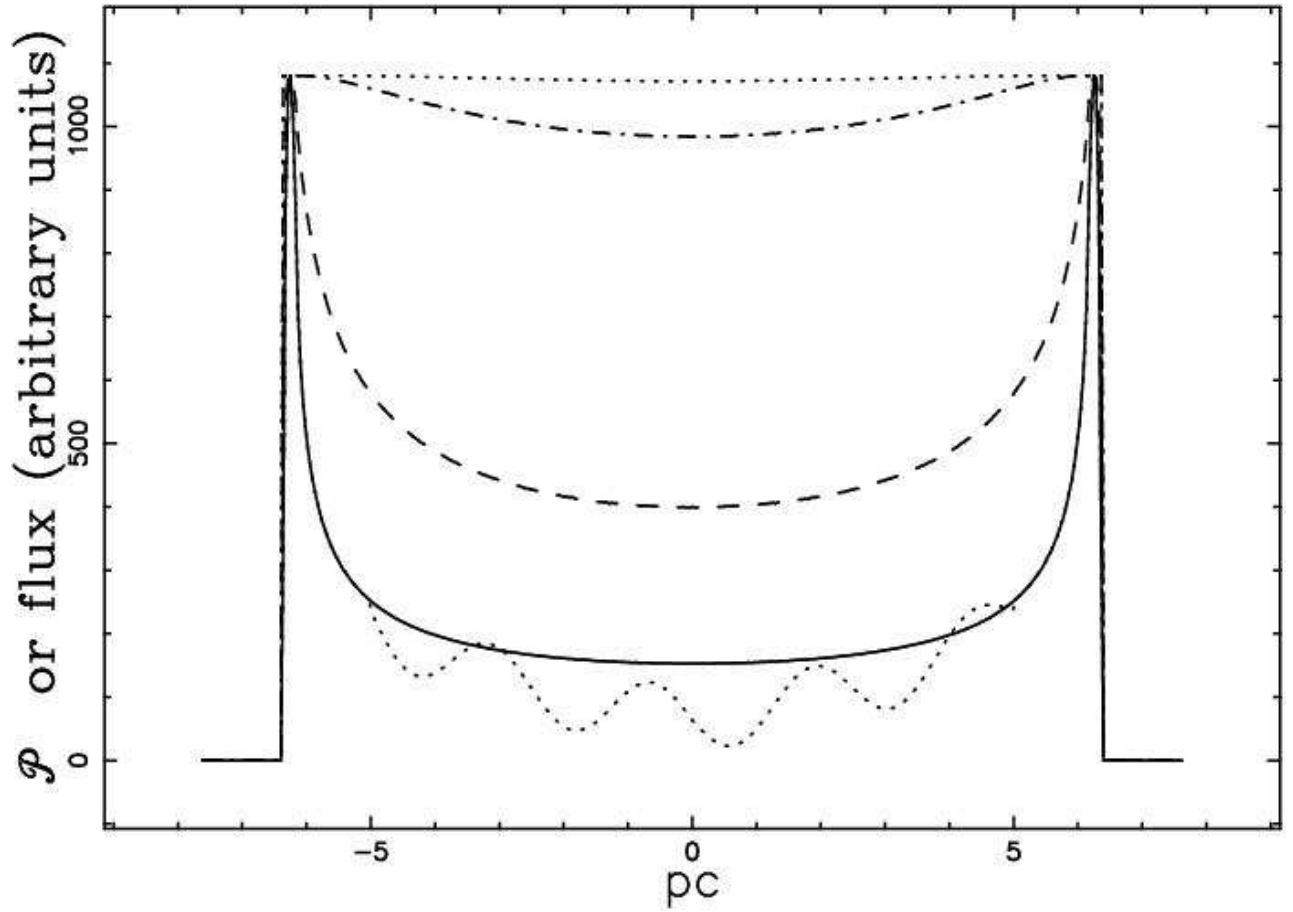


Figure 13: Cuts of the projection grid I crossing the center: X-ray data extracted from Dyer et al. (2004) (dashed thin line), $K_a = 10^{-2}$ (full line), $K_a = 1.8$ (dashed), $K_a = 10$ (dot-dash-dot-dash), $K_a = 20$ (dotted). Parameters as in Figure 10, great box. Transition from optically thin to thick layer.

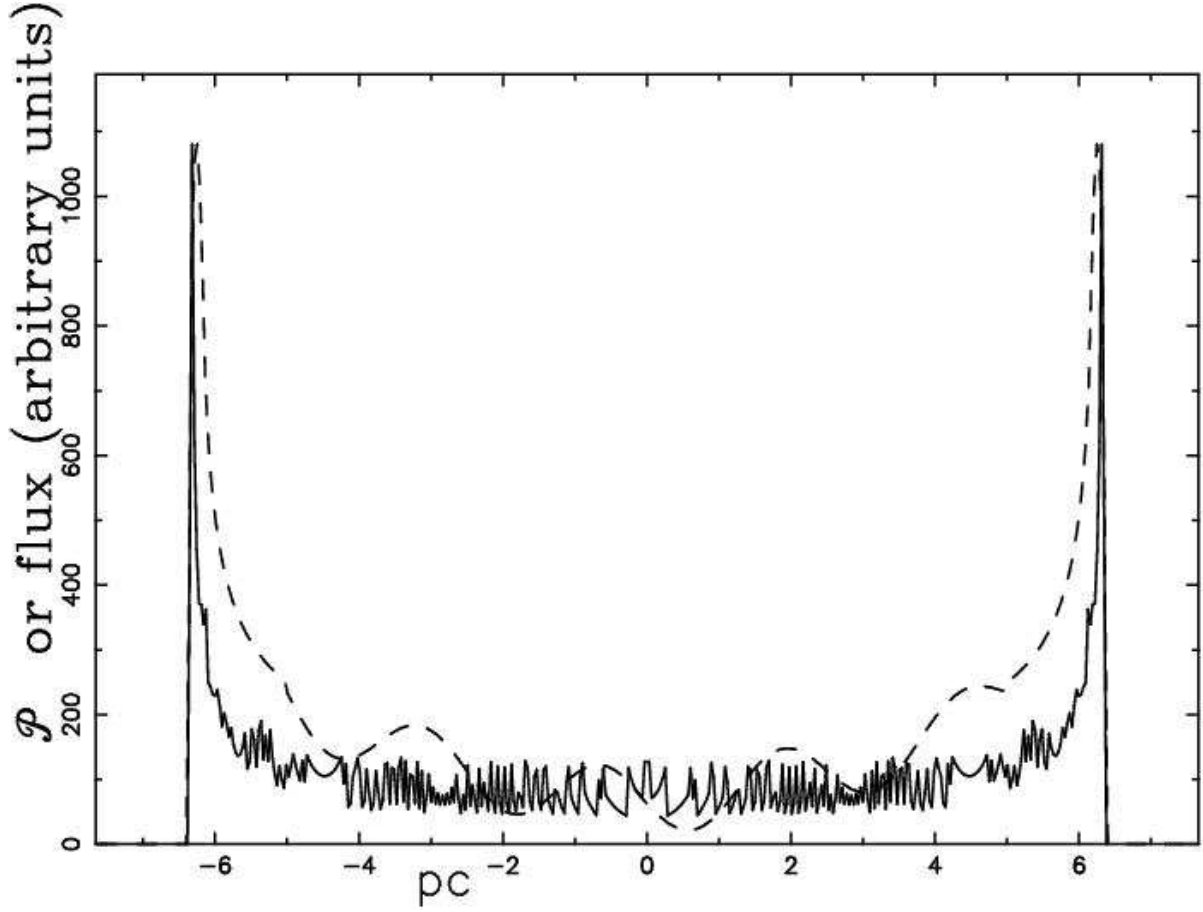


Figure 14: Cut of the mathematical intensity I crossing the center (full line) and X-ray data (dashed line) extracted from Dyer et al. (2004) . Parameters as in Table 2, $c_f=2$, but $H_4=1.2$. The simulation returns $W_u^{rw} = 1.17 \cdot 10^{-2} pc$ and $W_d^{rw} = 3.8 \cdot 10^{-2} pc$.

In the appendix A of a paper on X-ray synchrotron emission from SNR , Ballet (2006) , is possible to find a formula (analogous to our formula (74)) that gives the ratio between the brightness at the center of the sphere and at maximum ; his Figure A1 gives $\frac{flux_{ring}}{flux_{center}} \approx 3$.

6.5. The gamma emission

Up to now we have focused the attention on the X-ray emission from SNR ; the gamma ray emission ($30MeV < E < 30GeV$) is now analysed from two different points of view.

6.5.1. The gamma emission from relativistic electrons

Taking the lower limit of the gamma emission , $E=30$ Mev , the corresponding critical frequency is $\nu_c = 7.44 \cdot 10^{21}$ Hz and the relativistic gyro-radius with a magnetic field of $H_{-4}=1.2$, see Sect. 4.2.3, $\rho = 0.017$ pc. Due to the short time of synchrotron losses , $N=1$ collisions, the scale widths in the upstream and downstream direction are equal, $W_u = W_d = 0.037$ pc. In this case the simulation predicts a value given by $\frac{flux_{ring}}{flux_{center}} = 7.54$.

6.5.2. The gamma emission from cosmic rays

The cosmic rays with energy range $0.1 GeV < E < 410^5 GeV$, see Hillas (2005) and Wolfendale (2003) can produce gamma emission from the interaction with the target material. Once the CR energy is expressed in $10^{15}eV$ units (E_{15}) , the magnetic field in 10^{-6} Gauss (H_{-6}) the relativistic ion's gyro-radius is :

$$\rho_Z = 1.08 \frac{E_{15}}{H_{-6} Z} pc \quad , \quad (79)$$

where Z is the atomic number. The maximum energies that allow to apply the random walk of CR in shells of SNR are computed. The magnetic field of equipartition $H_6 = 15$, the minimum width of the X-profile , $W_u = 0.04$ pc and the proton , $Z = 1$, are selected. In order to sustain the random walk the following inequality should be verified

$$\rho_Z < W_u \quad , \quad (80)$$

that transformed in CR energy is

$$E_{15} < 0.55 \quad or \quad E < 5.5 \cdot 10^5 GeV \quad . \quad (81)$$

This upper limit is near to the maximum energy of CR that produces gamma radiation , $4 \cdot 10^5 GeV$. The various physical processes that allows to produce gamma radiation from CR are now summarised :

- Acceleration of CR at the shock discontinuity up to $E \approx 5 \cdot 10^5 GeV$,
- Diffusion of CR with step's length lower than W_u ,
- Absorption at W_u and W_d due to a change in the magnetic field from $H_4=0.15$ in the shell to $H_4=0.01$ outside the shell,

- Production of gamma radiation in a way proportional to the concentration of CR.

6.6. Asymmetric SNR

The theory of an asymmetric SNR was developed in Sect. 4.1 of Zaninetti (2000) in which an expansion surface as a function of a non-homogeneous ISM was computed: in the same paper Figure 8 models SN1006. The diffusing algorithm adopted here is the 3D random walk from many injection points (in the following IP)

1. The first IP is chosen
2. The first of the NPART electrons is chosen.
3. The random walk of an electron starts where the selected IP is situated. The electron moves in one of the six possible directions.
4. After N steps the process restarts from (2)
5. The number of visits is recorded on \mathcal{M}^3 , a three-dimensional grid.
6. The random walk terminates when all the NPART electrons are processed.
7. The process restarts from (1) selecting another IP
8. For the sake of normalisation the one-dimensional visitation/concentration grid \mathcal{M}^3 is divided by NPART.

The IP are randomly selected in space, and the radius is computed by using the method of bilinear interpolation on the four grid points that surround the selected latitude and longitude, (Press et al. (1992)). The radius will be the selected value + $R/24$ in order to generate the IP where the action of the shock is maximum.

Our model gives radial velocities, V_{theo} , $2211 \text{ km s}^{-1} \leq V_{theo} \leq 3580 \text{ km s}^{-1}$ and the map of the expansion velocity is reported in Figure 15 from which it is possible to visualise the differences in the expansion velocities among the various regions as well as the overall elliptical shape.

Before continuing we should recall that in the presence of discrete time steps on a 3D lattice the average square radius, $\langle R^2(N) \rangle$, after N steps (see Gould & Tobochnik (1988), equation (12.5)) is

$$\langle R^2(N) \rangle \sim 6DN \quad , \quad (82)$$

from which the diffusion coefficient, D , is derived

$$D = \frac{\langle R^2(N) \rangle}{6N} \quad . \quad (83)$$

The two boundaries in which the random walk is taking place are now represented by two irregular surfaces. It is possible to simulate them by stopping the random walk after a number of iterations N given by

$$N = NINT\left(\frac{\overline{R}_{pc}}{24} \frac{1}{\delta}\right)^2 \quad , \quad (84)$$

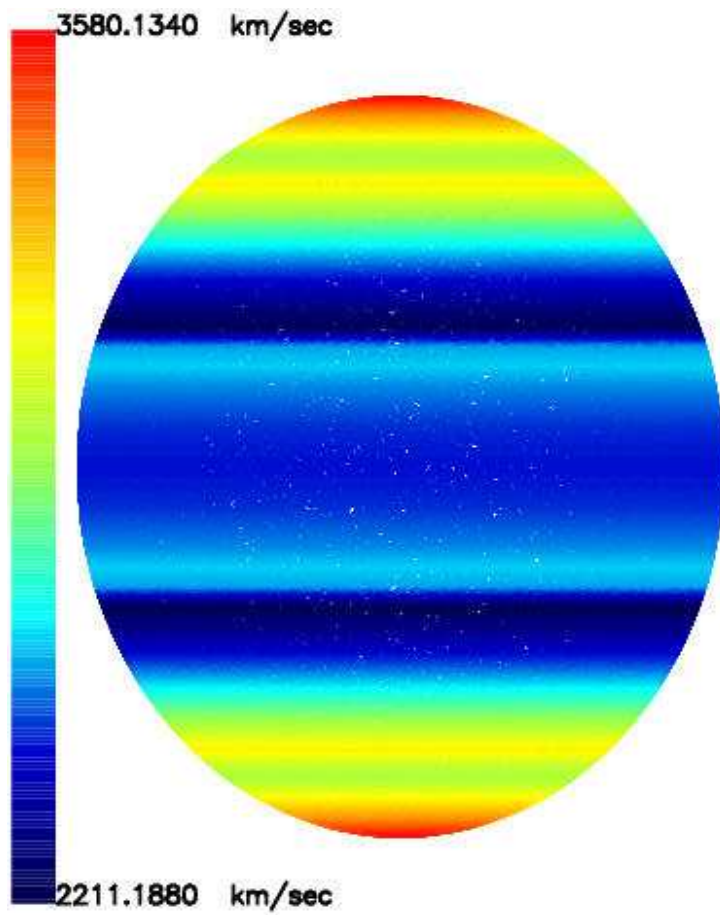


Figure 15: Map of the expansion velocity relative to the simulation of SNR1006 when 190000 random points are selected on the surface. The physical parameters are the same as in Figure 8 of Zaninetti (2000) .

where \overline{R}_{pc} represents the averaged radius in pc . These are the iterations after which according, to formula (83), the walkers reach the boundaries at a radial distance given by $\frac{\overline{R}_{pc}}{24}$ from the place of injection; in other words we are working on an unbounded lattice . The influence of velocity on the flux F of radiation can be inferred from the suspected dependence when non-thermal emission is considered, see equation (9.29) in McKee (1987) ,

$$F = \chi_t \frac{1}{4} \mu_H n_0 v_s^3 \quad , \quad (85)$$

where χ_T represents the efficiency of conversion of the unitarian flux of kinetic energy, μ_H the mass of the hydrogen nucleus, n_0 the particles/ cm^3 and v_s the velocity of the shock.

Assuming that the flux reversed in the non-thermal emission follows a similar law through the parameter χ_X (the efficiency in the X-region) the effect of velocity is simulated through the following algorithm. Once the IP are spatially generated, the number of times $NTIMES$ over which to repeat the cycle is given by

$$NTIMES = 1 + NTIMES_{MAX} * \left(\frac{v - v_{min}}{v_{max} - v_{min}} \right)^3 \quad , \quad (86)$$

where $NTIMES_{MAX}$ is the maximum of the allowed values of $NTIMES$ minus 1, and v is the velocity associated to each IP. The asymmetric contour map obtained when the spatial step is $\approx 2 * \text{gyro-radius}$ is reported in Figure 16 and the cut along two perpendicular lines of the projection grid in Figure 17.

In Figure 17 the asymmetry both in the peak to peak distance and the difference in the two maximum is evident. The ratio between the X-ray emission in the bright limbs (NE or SW) and toward the northwest or southeast (at 2 keV) is around 10 , see Figure 5 top right in Rothenflug et al. (2004) . Conversely our theoretical ratio , see Figure 17, is 9.84. It is also possible to plot the maximum of the theoretical intensity as function of the position angle , see Figure 18. The reader can make a comparison with the observational counterpart represented by Figure 5 top right, dashed line in Rothenflug et al. (2004) .

7. Conclusions

The results of astrophysical interest are now summarised:

1. A careful analysis of X-intensity of SNR near the external regions predicts a complex behaviour as given by the three equations (70), (71) and (72)); the fit with exponentials as adopted in Bamba et al. (2003) , our equation (10), is not supported by theoretical arguments.
2. The overall intensity profiles of SNR in the X-region, (represented by the new formulae (70), (71) and (72)) show a characteristic "U" shape that can be explained by the mathematical 3D diffusion. The predicted ratio between the intensity in the ring region and in the center region (7.15) is in agreement with the observations (5.4 -10.3).
3. The agreement between observed and theoretical overall "U" profiles allow us to exclude the presence of self-absorption (optically thick case), see simulation in Sect. 6.2.

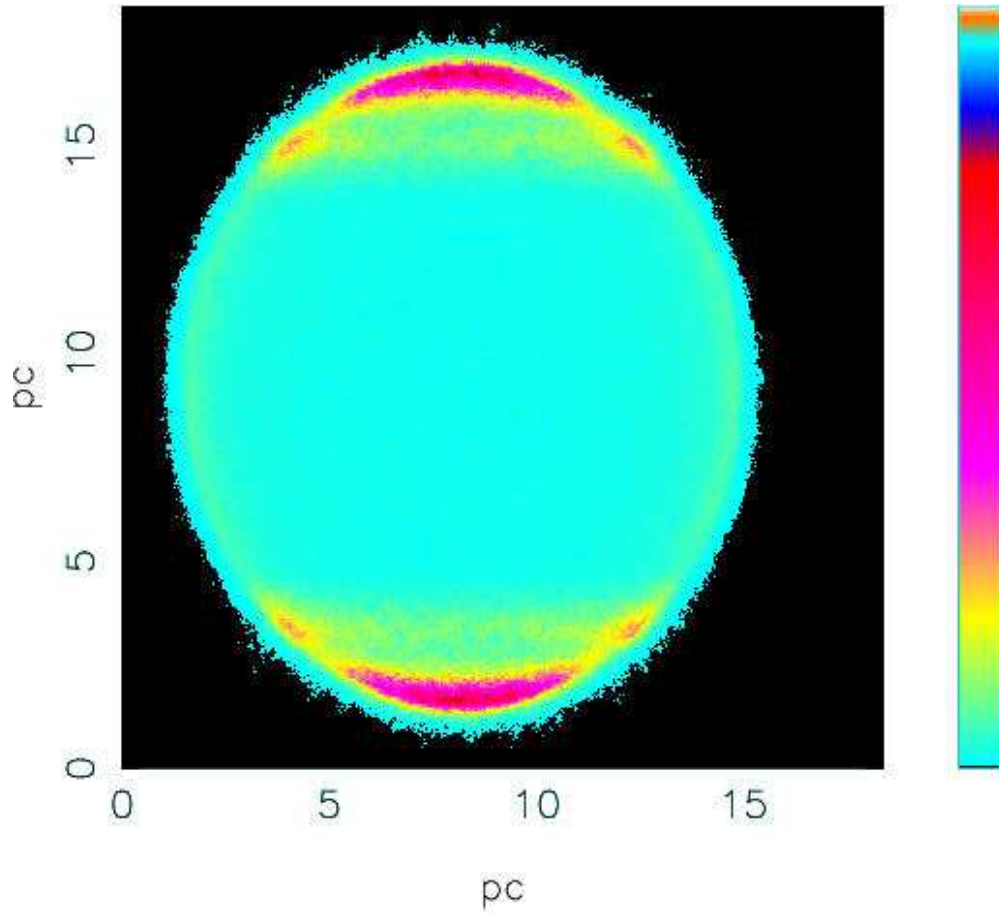


Figure 16: Contour of the intensity I in the X-rays. The parameters are $side_{SNR}=18.37$ pc, $\delta = 6.12 \cdot 10^{-3}$ pc, $\rho = 2.8 \cdot 10^{-3}$ pc, NDIM=3001, $IP = 190000^2$, $NPART=100$, $NTIMES_{max}=18$, great box. Optically thin layer.

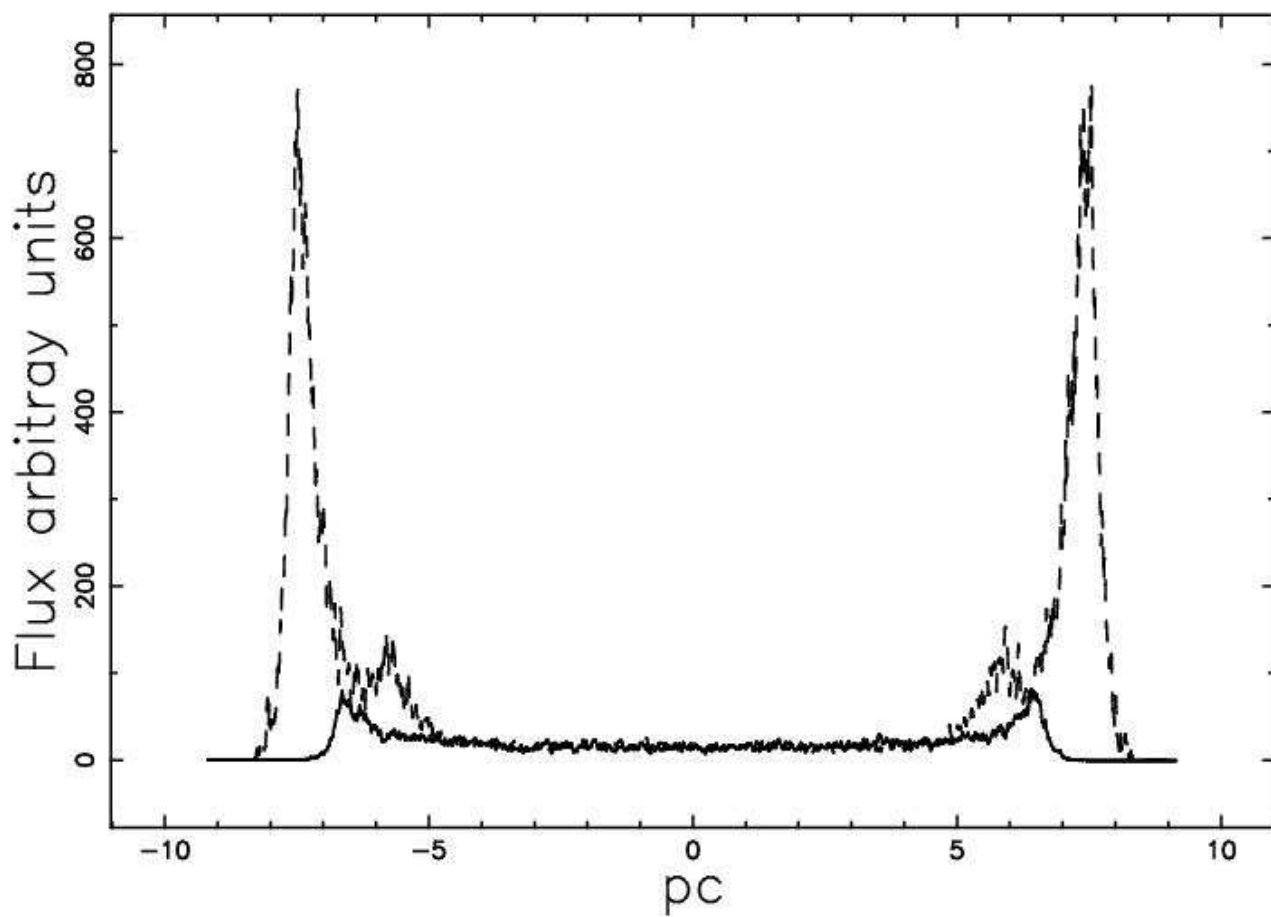


Figure 17: Two cut along perpendicular lines of I reported in Figure 16 . Optically thin layer.

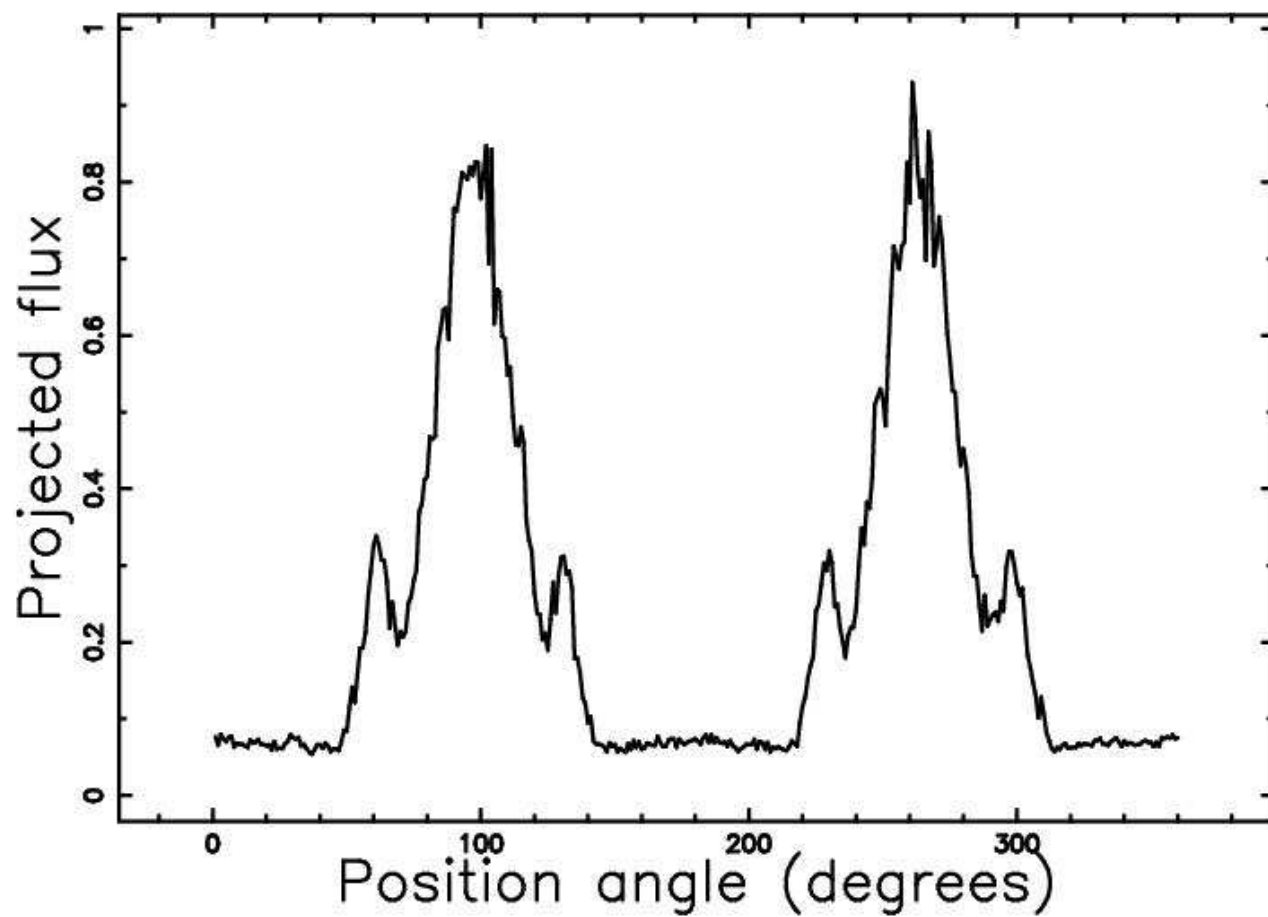


Figure 18: Azimuthal maximum of the profiles of intensity as function of the position angle in degrees. Same parameters as in Figure 16.

4. The Monte Carlo 1D random walk with length of the step as given by the Bohm diffusion provides the connection with the physical processes as well a new formula for the damping length (51), for the mean square displacement (61) and for the diffusion coefficient in the presence of drift (69). The mean square displacement, equation (61), turns out to be independent from the selected band of synchrotron emission. This independence explains the morphological similarities between the various regions of the e.m. spectrum in SNRs.
5. The SNR analysed here, SN1006, presents a spatial asymmetry at the northwest-southeast axis as well as a corresponding asymmetry in the flux. They can both be simulated once the concepts of diffusion from many injection points and variable flux of velocity are introduced, see Sect. 6.6.

The asymmetric random walk on an unbounded lattice in 1D once coupled with the concept of damping length can provide :

- a new way to deduce the magnetic field, $H_{-4}=1.2$, against $H_{-4}=0.15$ given by the equipartition arguments
- a reasonable explanation for the concentrations of relativistic electrons
- a value for the ratio between the intensity in the ring region and in the center region (6.88) which is in agreement with the observations (5.4 -10.3).

The analysis in the gamma region can be carried out splitting in two the analysis : gamma rays from synchrotron emission and gamma rays production in the interaction of CR with target material.

Eqs. (65)-(69) are strictly applicable only to non-relativistic plasma and the corresponding relativistic equations based on the first analyses of the theory of relativistic Brownian motion, can be considered a target for the future, see Dunkel & Hänggi (2005a), Dunkel & Hänggi (2005b), Dunkel & Hänggi (2006) and Dieckmann et al. (2006). A subject of further investigation is the role that the acceleration of electrons and cosmic rays plays on the shock jump conditions. According to McKee (1987) the key parameter is

$$w = \frac{p_{rs}}{p_s} \quad , \quad (87)$$

where p_{rs} is the post-shock pressure in relativistic particles and p_s is the post-shock pressure. The effect of the flow of energy from the shock to the relativistic particles is to reduce the temperature in the post-shock region and to modify the structure of the shock front.

ACKNOWLEDGEMENTS. The numerical code uses the subroutines extracted from "NUMERICAL RECIPES" for mathematical help. The plotting packages are PGPLOT 5.2 developed by T.J.Pearson and PGXTAL developed by D.S. Sivia.

Appendix A. Particle acceleration

The concept of stochastic acceleration started with the work by Fermi (1949) in which it was found that the collisions of a particle of energy E with a cloud

produced an average gain in energy (ΔE) proportional to the second order in u/c (u cloud velocity approaching that of light, c):

$$\left\langle \frac{\Delta E}{E} \right\rangle = \frac{8}{3} \left(\frac{u}{c} \right)^2 . \quad (88)$$

This process is named Fermi II.

On introducing an average length of collision λ , the formula becomes:

$$\frac{dE}{dt} = \frac{E}{\tau} , \quad (89)$$

where

$$\tau = \frac{4}{3} \left(\frac{u^2}{c^2} \right) \left(\frac{c}{\lambda} \right) . \quad (90)$$

It should be remembered that with a mean free path between clouds λ the average time between collisions with clouds is

$$2 \frac{\lambda}{c} , \quad (91)$$

see for example Lang (1999) (pag. 467) . This means that the particle reaches the cloud (our lattice point) in a time that is twice that of straight motion; it is therefore possible to speak of pseudo-rectilinear trajectories between the scatterer-clouds.

The probability, $P(t)$, that the particle remains in the reservoir for a period greater than t is now introduced,

$$P(t) = e^{-\frac{t}{T}} , \quad (92)$$

where T is the time of escape from the considered region. The hypothesis that energy is continuously injected in the form of relativistic particles with energy E_0 at the rate R , produces (according to Burn (1975)) the following probability density N , which is a function of the energy:

$$N(E) = \frac{R\tau}{E_0} \left(\frac{E}{E_0} \right)^{-\gamma} , \quad (93)$$

with

$$\gamma = 1 + \frac{\tau}{T} , \quad (94)$$

and τ is defined in (90) . Equation (93) can be written as

$$N(E) = K E^{-\gamma} , \quad (95)$$

where $K = \frac{R\tau}{E_0^{-\gamma+1}}$. A power law spectrum in the particle energy has now been obtained; it must be remembered that in this case the ratio of acceleration to escape time does not depend on particle energy.

The strong shock accelerating mechanism was later introduced by Bell (1978a) and Bell (1978b) ; the energy gain relative to a particle that is crossing the shock is:

$$\left\langle \frac{\Delta E}{E} \right\rangle = \frac{4}{3} \frac{u}{c} . \quad (96)$$

This process is named Fermi I; further on this process produces an energy spectrum of electrons of the type:

$$N(E)dE \propto E^{-2}dE \quad . \quad (97)$$

This allows us to postulate a kind of universal mechanism that produces synchrotron radiation with intensity $I(\nu) \propto \nu^{-0.5}$.

It is interesting to point out that the index γ of the accelerated particles depends on the parameters of the shocks u and L , where L represents the thickness and u the velocity of the shocks. In particular when $u < \frac{D}{L}$ where D is the spatial diffusion coefficient, the spectrum of accelerated particles becomes very soft, see Figure 3 by Ostrowski & Schlickeiser (1996). The quoted standard spectral index of -2 adopted here for the electrons is calculated without escape boundaries assuming that there is an infinite box; Ostrowski & Schlickeiser (1996) added the possibility of escape and showed its effect on the solution.

Appendix B. The adiabatic losses

Other types of losses are those due to adiabatic cooling, see e.g. Downes et al. (2002), which affects all electron energies and not just the highest ones as in synchrotron cooling. Following the approach of Longair (1994) (equation (19.5)), they are

$$-\frac{1}{E}\left(\frac{dE}{dt}\right)_{ad} = \left(\frac{1}{R}\frac{dR}{dt}\right) = \frac{1}{t_{exp}} \quad (98)$$

where R is the radius of the SNR and t_{exp} is the characteristic time of expansion. The adiabatic losses are negligible if the time scale of the expansion t_{exp} defined in equation (98) is greater than the time, t_{rw} , the relativistic particles have been in the emitting shell:

$$t_{exp} \gg t_{rw} \quad . \quad (99)$$

In the case of SNR, the analytical solution for the radius can be found in McCray (1987), equation (10.27):

$$R(t) = \left(\frac{25E_{expl}t_{SNR}^2}{4\pi\zeta_0}\right)^{1/5} \quad , \quad (100)$$

where ζ_0 is the density of the surrounding medium which is supposed to be constant, E_{expl} is the energy of the explosion, and t_{SNR} is the age of the SNR. One should note that this is a Sedov solution, while SN 1006 is young and not described by Sedov's formulae. Self-similar solutions for this stage of evolution were proposed by Nadezhin (1981), Nadezhin (1985) and Chevalier (1982). Upon inserting equation (100) in equation (98), the time scale of the expansion takes the simple form

$$t_{exp} = \frac{5}{2}t_{SNR} \quad . \quad (101)$$

Sect. 4.1 shows that with our choice of parameters the inequality given by equation (99) is always verified; therefore the adiabatic losses can be neglected.

REFERENCES

- Axford W. I., Leer E., Skadron G. 1978, in International Cosmic Ray Conference , p. 132
- Ballet J. 2006, Advances in Space Research , 37 , 1902
- Bamba A., Yamazaki R., Ueno M., Koyama K. 2003, ApJ , 589, 827
- Bell A. R. 1978a, MNRAS , 182, 147
- Bell A. R. 1978b, MNRAS , 182, 443
- Berezinskii V. S., Bulanov S. V., Dogiel V. A., Ptuskin V. S. 1990, Astrophysics of cosmic rays, North-Holland, Amsterdam
- Berg H. C. 1993, Random Walks in Biology, Princeton University Press, Princeton
- Blandford R. D., Ostriker J. P. 1978, ApJ , 221, L29
- Bohm D., Burhop E., Massey H., 1949, in Characteristic of Electrical Discharges in Magnetic Fields, McGraw-Hill, New-York
- Burn B. J. 1975, A&A , 45, 435
- Chevalier R. A. 1982, ApJ , 258, 790
- Crank J. 1979, Mathematics of Diffusion, Oxford University Press, Oxford
- Dieckmann M. E., O'C Drury L., Shukla P. K. 2006, New Journal of Physics, 8, 40
- Downes T. P., Duffy P., Komissarov S. S. 2002, MNRAS , 332, 144
- Drury L. O. 1983, Reports of Progress in Physics, 46, 973
- Dunkel J., Hänggi P., 2005a, Phys. Rev. E, 71, 016124
- Dunkel J., Hänggi P., 2005b, Phys. Rev. E, 72, 036106
- Dunkel J., Hänggi P., 2006, Phys. Rev. E, 74, 051106
- Dyer K. K., Reynolds S. P., Borkowski K. J., 2004, ApJ , 600, 752
- Ellison D. C., Berezhko E. G., Baring M. G., 2000, ApJ , 540, 292
- Ellison D. C., Reynolds S. P., 1991, ApJ , 382, 242
- Ellison D. C., Reynolds S. P., Borkowski K. et al. 1994, PASP, 106, 780
- Ellison D. C., Reynolds S. P., Jones F. C. 1990, ApJ , 360, 702
- Ellison D. C., Slane P., Gaensler B. M. 2001, ApJ , 563, 191
- Fermi E. 1949, Physical Review, 75, 1169
- Ferraro M., Zaninetti L. 2001, Phys. Rev. E, 64, 056107
- Ferraro M., Zaninetti L. 2004, Physica A, 338, 307
- Gould H., Tobochnik J. 1988, An introduction to computer simulation methods, Addison-Wesley, Reading, Menlo Park
- Gustafson K. E. 1980, Partial Differential equations and Hilbert Space Methods, John Wiley and Sons, New York
- Hillas A. M. 2005, J. Phys. G , 31, 95
- Hjellming R. M. 1988, Radio stars. Galactic and Extragalactic Radio Astronomy, p. 381
- Jokipii J. R. 1987, ApJ , 313, 842
- Kirk J. G. 1994, in Benz A. O., Courvoisier T. J.-L., eds, Saas-Fee Advanced Course 24: Plasma Astrophysics Particle Acceleration . p. 225

- Klepach E. G., Ptuskin V. S., Zirakashvili V. N. 2000, *Astroparticle Physics*, 13, 161
- Krymskii G. F., 1977, *Akademiia Nauk SSSR Doklady*, 234, 1306
- Lang K. R., 1999, *Astrophysical formulae*, Springer, New York
- Longair M. S., 1994, *High energy astrophysics*, Cambridge University Press, 2nd ed., Cambridge
- McCray R. 1987 In: *Spectroscopy of astrophysical plasmas*, eds. Dalgarno A., Layzer D., Cambridge University Press, Cambridge
- McKee C. F. 1987 In: *Spectroscopy of astrophysical plasmas*, eds. Dalgarno A., Layzer D., Cambridge University Press, Cambridge
- Morse P. H., Feshbach H. 1953, *Methods of Theoretical Physics*, Mc Graw-Hill Book Company, New York
- Nadezhin D. K. 1981, Preprint ITEP-1
- Nadezhin D. K. 1985, *Astrophysics and Space Science*, 112, 225
- Ostrowski M., Schlickeiser R. 1996, *Sol. Phys.*, 167, 381
- Pacholczyk A. G. 1970, *Radio astrophysics. Nonthermal processes in galactic and extragalactic sources*, Freeman, San Francisco
- Parker E. N. 1958, *Physical Review*, 109, 1328
- Parker E. N. 1965, *Planet. Space Sci.*, 13, 9
- Press W. H., Teukolsky S. A., Vetterling W. T., Flannery B. P., 1992, *Numerical recipes in FORTRAN. The art of scientific computing*, Cambridge University Press, Cambridge
- Reynolds S. P. 1998, *ApJ*, 493, 375
- Rothenflug R., Ballet J., Dubner G., Giacani E., Decourchelle A., Ferrando P. 2004, *A&A*, 425, 121
- Rybicki G., Lightman A. 1985, *Radiative Processes in Astrophysics*, Wiley-Interscience, New-York
- Schlickeiser R. 2002, *Cosmic ray astrophysics*, Springer, Berlin
- Skilling J. 1975, *MNRAS*, 172, 557
- Strom R. G. 1988, *MNRAS*, 230, 331
- Vainio R., Schlickeiser R. 1998, *A&A*, 331, 793
- Völk H. J., Berezhko E. G., Ksenofontov L. T. 2005, *A&A*, 433, 229
- Wolfendale A. W. 2003, *J. Phys. G*, 29, 787
- Zaninetti L. 2000, *A&A*, 356, 1023